Asian Journal of Chemistry; Vol. 38, No. 11 (2026), 2947-2967
ASIAN JOURNAL OF CHEMISTRY
https://doi.org/10.14233/ajchem.2026.36830

Experimental and Theoretical Insights into Structural, Spectroscopy, DFT and Biological Activity of 5-Fluorouracil Thiourea Cocrystal

JAYAPRIYANGA KARUPPASAMY[1], SANDHYARANI REBBAVARAPU[2], AZAR ZOCHEDH[3,*], BHARATHI MURUGANANTHAM[4] and ASATH BAHADUR SULTAN[1,*]

[1]Condensed Matter Physics Laboratory, Department of Physics, International Research Center, Kalasalingam Academy of Research and Education, Krishnankoil-626126, India
[2]Department of Biotechnology, University Institute of Emerging Technologies, Guru Nanak University, Ibrahimpatnam-501506, India
[3]Department of Computational Biology, Saveetha School of Engineering, Saveetha Institute of Medical and Technical Sciences (SIMATS), Saveetha University, Chennai-602105, India
[4]Center for Bioinformatics, Department of Biochemistry, Karpagam Academy of Higher Education, Coimbatore-641021, India

*Corresponding authors: E-mail: azar2411@gmail.com; s.asathbahadur@gmail.com

Received: 14 July 2026 *Accepted*: 6 October 2026 *Published online*: 13 November 2026 AJC-22526

A cocrystal of the anticancer drug 5-fluorouracil with thiourea (5FUTU) was synthesized and single crystal was grown by slow solvent evaporation. Single-crystal X-ray diffraction (SCXRD) established the unit cell parameters and powder X-ray diffraction (PXRD) confirmed the formation and phase purity of the cocrystalline phase. Hirshfeld surface analysis and the associated two-dimensional fingerprint plots were used to identify the intermolecular interactions governing crystal packing and to quantify their relative contributions. The functional groups in 5FUTU were characterized by Fourier-transform infrared (FTIR) spectroscopy and its electronic absorption behaviour was examined by UV-Vis spectroscopy. Density functional theory (DFT) calculations were performed to support the experimentally determined crystal structure and to elucidate the spectroscopic and electronic properties of the cocrystal. The calculations included frontier molecular orbital (HOMO-LUMO) energies, natural and Mulliken population analyses, Fukui functions to gain further insight into its electronic distribution, chemical reactivity and stability. The biological potential of 5FUTU was evaluated by molecular docking and an *in vitro* MTT cytotoxicity assay. Molecular docking revealed favourable binding of 5FUTU to glycogen synthase kinase-3β (GSK-3β), with a binding energy of -6.6 kcal/mol. The MTT assay showed cytotoxic activity against MDA-MB-231 breast cancer cells, with an IC_{50} of 46.7 μM. Pharmacokinetic analysis assessed its drug-likeness and support further investigation of 5FUTU in structure-based drug design for breast cancer therapy.

Keywords: Cocrystal, 5-Fluorouracil, Thiourea, Molecular docking, Bioactivity, MDA-MB-231 cells.

INTRODUCTION

The development of novel anticancer agents remains a priority due to cancer's global burden and the toxicity of existing chemotherapies. Structural modification of established pharmacophores can improve biological activity and pharmacokinetic properties. Nitrogen-containing heterocycles are widely investigated for their potential anticancer activity and interactions with biological targets [1-3]. Among these compounds, 5-fluorouracil (5-FU), a fluorinated pyrimidine antimetabolite, has been widely used in the treatment of several malignancies, including colorectal, breast, brain and skin cancers [4-7]. However, its clinical efficacy is limited by factors such as variable therapeutic response, toxicity and the development of drug resistance. Although combination chemotherapy can improve treatment outcomes, its effectiveness depends on the drugs and cancer types involved [8]. Consequently, chemical derivatization of 5-FU remains an important approach for modifying its physico-chemical properties and exploring improved anticancer activity. Nevertheless, the conventional synthetic routes may involve multiple reaction and purification steps, generating chemical waste and increasing solvent and reagent consumption. These limitations highlight the need for efficient and environmentally benign

This is an open access journal, and articles are distributed under the terms of the Attribution 4.0 International (CC BY 4.0) License. This license lets others distribute, remix, tweak, and build upon your work, even commercially, as long as they credit the author for the original creation. You must give appropriate credit, provide a link to the license, and indicate if changes were made.

synthetic strategies that enable the preparation of 5-FU derivatives with reduced processing requirements and potentially improved biological properties.

Cocrystallization has emerged as a promising crystal-engineering strategy for modifying the physico-chemical properties of pharmaceutical compounds and potentially improving their solubility, permeability and bioavailability [9]. Several cocrystals and adducts of 5-FU have been reported with coformers such as 3-hydroxybenzoic acid, 4-aminobenzoic acid and cinnamic acid with enhanced permeability [10]. Other reported systems include 5-FU adducts with acridine, phenazine, 4,4′-bispyridylethene, 4-methylbenzoic acid, 3-aminobenzoic acid, gentisic acid, 3,4-dihydroxybenzoic acid and *p*-aminopyridine [11,12]. Cocrystal formation with cinnamic acid, succinic acid, malic acid and benzoic acid has also been investigated to improve pharmaceutical performance [13]. In addition, 5-FU adducts with urea, thiourea, 2,2′-bipyridine and 4,4′-bipyridine have been investigated for their potential anticancer properties using molecular docking [14]. The crystal structure of the 5-fluorouracil-thiourea cocrystal (5FUTU) has been previously reported [14]. Therefore, this study focuses on an integrated analysis of its molecular, solid-state, electronic and biological properties, correlating crystallographic data, spectroscopic characteristics, intermolecular interactions, crystal-packing energetics, protein binding and *in vitro* cytotoxicity against breast cancer cells.

Moreover, this study aims to validate the reported 5FUTU crystal form and investigate its structural, spectroscopic, electronic and biological properties using experimental and computational approaches. X-ray diffraction, FTIR, UV-Vis, and NMR spectroscopy were combined with DFT, intermolecular interaction analyses and crystal-packing energy calculations. The molecular docking and MTT assays using MDA-MB-231 breast cancer cells were employed to explore protein-binding interactions and cytotoxicity. The novelty lies in integrating these findings to establish structure–property relationships and assess the biological potential of the previously reported 5FUTU crystal form, rather than claiming a new crystal structure.

EXPERIMENTAL

5-Fluorouracil (≥ 98%) and thiourea (AR grade, 99.5%) were purchased from Sigma-Aldrich, India and used as received without further purification. Ethanol and deionized water were used as solvents for cocrystal growth.

Growth of 5FUTU crystals: 5-Fluorouracil (130.08 g/mol) and thiourea (76.12 g/mol) were weighed in a 1:1 molar ratio and ground together thoroughly. The 5FUTU cocrystal was prepared by liquid-assisted grinding with ethanol and the product was dried at 50 ºC for 1 h. Single crystals of 5FUTU were grown by slow evaporation following a reported procedure [14]. The crystals obtained were small but of sufficient size and quality for single-crystal X-ray diffraction analysis.

Characterization: Powder X-ray diffraction (PXRD) patterns were recorded on a Bruker D8 Advance ECO diffrac-tometer using Cu*K*α radiation (λ = 1.5405 Å) over the 2θ range 20-80º. The unit cell parameters and the triclinic space group were determined by single-crystal X-ray diffraction on a Bruker AXS Kappa APEX-II diffractometer. The functional groups in the cocrystal were identified by Fourier-transform infrared (FTIR) spectroscopy on a Shimadzu IRTracer-100 spectrometer over 4000-400 cm^{-1}. ^{1}H and ^{13}C NMR spectra of 5FUTU were recorded on a Bruker Avance III HD Nanobay 400 MHz FT-NMR spectrometer. The UV-visible transmission spectrum was recorded on a Shimadzu UV-1700 spectrophotometer over 200-500 nm.

Quantum chemical analysis: All quantum chemical calculations on 5FUTU were performed with the Gaussian 09 software package [15] and the results were visualized using GaussView [16]. The molecular geometry of 5FUTU was optimized by density functional theory (DFT) using the B3LYP hybrid functional with the 6-311++G (d, p) basis set [17,18]. The vibrational assignments were performed using potential energy distribution (PED) analysis with VEDA 4 [19] and calculated frequencies were scaled to account for anharmonicity and basis-set limitations [20]. Natural bond orbital (NBO) analysis was conducted using NBO 3.1 in Gaussian 09 [21]. The HOMO and LUMO energies were used to estimate the ionization potential (I) and electron affinity (A) based on Koopmans' theorem [22]. Global hardness, softness, electronegativity and chemical reactivity descriptors were also derived from the DFT results [23].

Molecular docking: The three-dimensional structures of the target proteins were retrieved from the RCSB Protein Data Bank (https://www.rcsb.org/). Protein preparation was performed using BIOVIA Discovery Studio 2021 Client by removing water molecules, heteroatoms, and co-crystallized ligands. Molecular docking of 5FUTU was conducted using PyRx 0.8. Binding affinities were evaluated and the resulting protein-ligand complexes were visualized in BIOVIA Discovery Studio to identify interacting residues, interaction types, and bond distances.

MTT evaluation: The cytotoxicity of 5FUTU against MDA-MB-231 triple-negative breast cancer cells was evaluated using the MTT assay. The cells, obtained from NCCS, Pune, were cultured in Dulbecco's Modified Eagle Medium (DMEM) supplemented with 10% fetal bovine serum (FBS) and penicillin-streptomycin at 37 °C under 5% CO_2. After 24 h of incubation, the cells were treated with different concentrations of 5FUTU, with free 5-fluorouracil (5-FU) serving as a comparator. Following 24 h of treatment, MTT solution was added and the cells were incubated in the dark for 3 h. Dimethyl sulfoxide (DMSO) was then added to dissolve the formazan crystals formed by viable cells. The absorbance was measured at 575 nm and cell viability was calculated as a percentage using the following formula:

$$\frac{\text{Abs of treated cells}}{\text{Abs of control cells}} \times 100$$

Pharmacokinetic analysis: The pharmacokinetic profiles of 5-FU and the 5FUTU cocrystal were evaluated *in silico* using SwissADME (http://www.swissadme.ch/) based on their SMILES structures. Physicochemical properties, pharmacokinetic parameters, cytochrome P450 inhibition, P-glycoprotein interactions, water solubility and synthetic accessibility were assessed. The results were compared to examine the potential influence of cocrystal formation on the predicted drug-like properties and pharmacokinetic profiles.

RESULTS AND DISCUSSION

Molecular structural parameters: The 5FUTU cocrystal was characterized by single-crystal X-ray diffraction (SCXRD), yielding unit-cell parameters of attained as a = 6.1632 Å, b = 7.1102 Å, c = 10.661 Å, α = 101.947º, β = 98.244º and γ = 114.211º with $P\bar{1}$ space group These parameters agree with the previously reported crystallographic data [14]. The experimental powder X-ray diffraction (PXRD) pattern was compared with the pattern simulated from the single-crystal data, with good agreement between the two profiles (Fig. 1). This comparison supports the phase identity of the synthesized cocrystal.

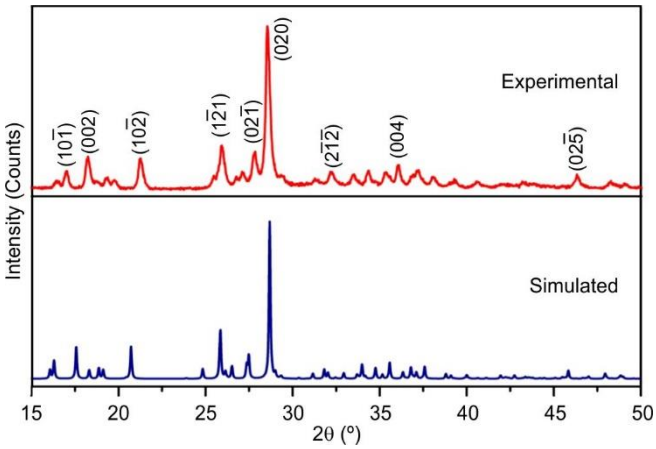


Fig. 1. Powder XRD patterns of 5FUTU cocrystal

The molecular geometry of 5FUTU was optimized at the DFT/B3LYP/6-311++G(d,p) level of theory. The optimized structure and atom numbering are shown in Fig. 2. The calculated total energy was -1062.5150 a.u. The optimized bond lengths, bond angles and dihedral angles were compared with the experimental crystallographic values reported in the literature [14]. Differences between the calculated and experimental parameters are expected as the theoretical calculations describe the molecule in the gas phase, whereas the experimental geometry is governed by the solid-state environment and intermolecular interactions.

Within the 5-fluorouracil moiety, the mean C–N bond length of the pyrimidine ring was 1.389 Å from DFT calculations and 1.368 Å experimentally. The calculated C–C and C=C bond lengths were 1.3441 and 1.4561 Å, respectively,

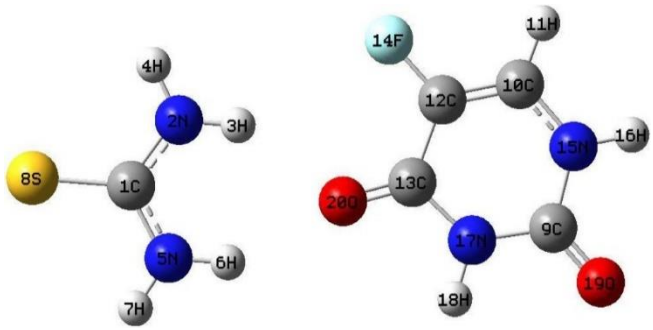


Fig. 2. Optimized molecular structure and atomic numbering of 5FUTU cocrystal

compared with experimental values of 1.335 and 1.432 Å. The C–F bond length was 1.341 Å theoretically and 1.347 Å experimentally. The mean carbonyl C=O bond length was 1.214 Å from DFT calculations, compared with 1.235 Å in the crystal structure (Table-1).

The mean C–N–C bond angle was 126.163º theoretically and 125.0º experimentally. The corresponding calculated and experimental values for the mean C–C–N, C–N–O and C–C–F angles were 116.64º; and 116.65º, 123.59º and 122.65º; and 119.21º and 119.1º, respectively. The mean N–C–O angle was 123.03º theoretically and 122.1º experimentally, while the C–C–O angle was 125.345º and 125.5º, respectively (Table-2). The small differences between the calculated and experimental values support the consistency of the optimized geometry with the reported crystal structure. The pyrimidine ring was nearly planar, with minimal deviations in its dihedral angles. The hydrogen, oxygen and fluorine atoms attached to the ring remained close to the ring plane (Table-3).

For the thiourea moiety, the mean C–N bond length was 1.3556 Å from DFT calculations and 1.332 Å experimentally. The corresponding N–H bond lengths were 1.008 and 0.88 Å. The C–S bond length was calculated as 1.6839 Å as compared with the experimental value of 1.707 Å. The mean N–C–S bond angle was 122.56º theoretically and 120.75º experimentally, while the N–C–N angle was 115.11º and 118.5º, respectively. The calculated bond angles were generally close to their experimental counterparts, although some deviations were observed. Dihedral-angle analysis established a nearly planar arrangement of the thiourea moiety, with a maximum deviation of approximately 1.4º. The DFT analysis confirmed the presence of an intermolecular N2–H3···O20 hydrogen bond in 5FUTU.

TABLE-1
BOND LENGTH (Å) IN 5-FLUOROURACIL THIOUREA COCRYSTAL

Atoms	DFT	Expt. [14]	Atoms	DFT	Expt. [14]
C1-N2	1.3545	1.333(3)	C10-H11	1.0817	0.95
C1-N5	1.3565	1.330(2)	C10-C12	1.3441	1.335(3)
C1-S8	1.6839	1.707(2)	C10-N15	1.3755	1.366(2)
N2-H3	1.0112	0.88	C12-C13	1.4561	1.432(3)
N2-H4	1.0047	0.88	C12-F14	1.3405	1.347(2)
N5-H6	1.0099	0.88	C13-N17	1.3951	1.374(2)
N5-H7	1.0047	0.88	C13-O20	1.2195	1.238(2)
C9-N15	1.3901	1.354(3)	N15-H16	1.0096	0.88
C9-N17	1.3944	1.379(2)	N17-H18	1.0134	0.88
C9-O19	1.2082	1.231(2)			

TABLE-2
BOND ANGLE (º) IN 5-FLUOROURACIL THIOUREA COCRYSTAL

Atoms	DFT	Expt. [14]	Atoms	DFT	Expt. [14]
N2-C1-N5	115.1105	118.5(2)	C12-C10-N15	120.5219	119.9(2)
N2-C1-S8	122.5613	121.7(2)	C10-C12-C13	121.5749	121.8(2)
N5-C1-S8	122.5613	119.8(1)	C10-C12-F14	121.3728	121.1(2)
C1-N2-H3	121.9068	120	C13-C12-F14	117.0523	117.1(2)
C1-N2-H4	117.771	120	C12-C13-N17	112.7548	113.4(2)
H3-N2-H4	120.3222	120	C12-C13-O20	125.3447	125.5(2)
C1-N5-H6	121.9797	120	N17-C13-O20	121.9005	121.0(2)
C1-N5-H7	117.7271	120	C9-N15-C10	123.9632	123.3(2)
H6-N5-H7	120.2932	120	C9-N15-H16	115.3967	118.3
N15-C9-N17	112.8219	114.8(2)	C10-N15-H16	120.6401	118.3
N15-C9-O19	123.5225	123.1(2)	C9-N17-C13	128.3631	126.7(2)
N17-C9-O19	123.6556	122.2(2)	C9-N17-H18	115.2152	116.7
H11-C10-C12	122.1638	120.1	C13-N17-H18	116.4217	116.6
H11-C10-N15	117.3143	120			

TABLE-3
TORSIONAL ANGLE (º) IN 5-FLUOROURACIL THIOUREA COCRYSTAL

Atoms	DFT	Expt. [14]	Atoms	DFT	Expt. [14]
N5-C1-N2-H3	0.0304	0	H11-C10-C12-C13	-179.9999	-179.8
N5-C1-N2-H4	179.965	180	H11-C10-C12-F14	0.0006	-0.3
S8-C1-N2-H3	-179.972	-178.6	N15-C10-C12-C13	-0.0001	0.2(3)
S8-C1-N2-H4	-0.0375	1.4	N15-C10-C12-F14	180.0004	179.7(2)
N2-C1-N5-H6	0.0003	0	H11-C10-N15-C9	-179.9993	-178.9
N2-C1-N5-H7	179.9819	180	H11-C10-N15-H16	-0.0008	1.1
S8-C1-N5-H6	-179.9973	178.7	C12-C10-N15-C9	0.0008	1.1(3)
S8-C1-N5-H7	-0.0157	-1.4	C12-C10-N15-H16	179.9993	-178.9
C1-N2-O20-C13	179.9995	–	C10-C12-C13-N17	0.0	-0.5(3)
H4-N2-O20-C13	0.065	–	C10-C12-C13-O20	179.9999	179.0(2)
N17-C9-N15-C10	-0.0013	-1.9(3)	F14-C12-C13-N17	179.9995	179.9(2)
N17-C9-N15-H16	-179.9999	178.1	F14-C12-C13-O20	-0.0006	-0.5(3)
O19-C9-N15-C10	179.9988	178.7(2)	C12-C13-N17-C9	-0.0006	-0.4(3)
O19-C9-N15-H16	0.0003	-1.3	C12-C13-N17-H18	180.001	179.6
N15-C9-N17-C13	0.0012	1.5(3)	O20-C13-N17-C9	-180.0005	-179.9(2)
N15-C9-N17-H18	-180.0004	-178.5	O20-C13-N17-H18	0.0011	0.1
O19-C9-N17-C13	180.0011	-179.0(2)	C12-C13-O20-H3	-0.0008	–
O19-C9-N17-H18	-0.0005	1	N17-C13-O20-H3	-180.0009	–

Hirshfeld surface studies: Hirshfeld surface analysis was performed using CrystalExplorer 3.1 to examine the intermolecular interactions responsible for crystal packing in the 5FUTU cocrystal. The normalized contact distance (d_{norm}), external distance (d_e) and internal distance (d_i) surfaces were used to visualize the contacts between neighbouring molecules (Fig. 3). In the d_{norm} surface, red regions indicate contacts shorter than the sum of the van der Waals radii, white regions represent contacts close to van der Waals separation and blue regions correspond to longer contacts. The d_{norm}, d_e and d_i values were mapped over the ranges of -0.68 to 1.2, 0.73 to 2.4 and 0.73 to 2.3 a.u., respectively. The shape-index and curvedness surfaces were also examined to identify possible π–π stacking interactions. The calculated Hirshfeld surface area and volume were 209.68 Å^2 and 192.25 Å^3, respectively.

The 2D fingerprint plots provide a quantitative assessment of the intermolecular contacts in the 5FUTU cocrystal (Fig. 4). The fingerprint plot (Fig. 4a) shows the relative contributions of different contacts to the Hirshfeld surface. O···H/H···O contacts account for 22.5% of the surface and represent the largest contribution among the reported interactions [24]. The H···H contacts contribute 19.0%, while F···H, C···H and N···H contacts account for 14.3%, 7.8% and 6.1%, respectively. Other contacts including C···C (3.5%), O···O (2.0%), O···C (1.6%), C···S (1.5%), N···N (1.5%) and S···S (1.1%), make smaller contributions. The sharp spikes in the fingerprint plots correspond to O···H/H···O contacts and indicate close intermolecular interactions involving hydrogen and oxygen atoms. The N–H wings may be associated with N–H···π interactions, while the shape-index and curvedness surfaces provide additional evidence for possible π–π stacking. These features help explain the intermolecular contacts that contribute to the crystal packing of 5FUTU.

The atom-pair contact analysis further illustrates the distribution of intermolecular interactions across the Hirshfeld surface (Fig. 5a). H···ALL contacts account for 51.9% of the total contacts, which indicate the substantial contribution of hydrogen involving interactions to the crystal packing. The corresponding contributions from C···ALL, F···ALL, N···ALL, O···ALL and S···ALL contacts are 6.2%, 14.3%, 10.1%, 9.5%

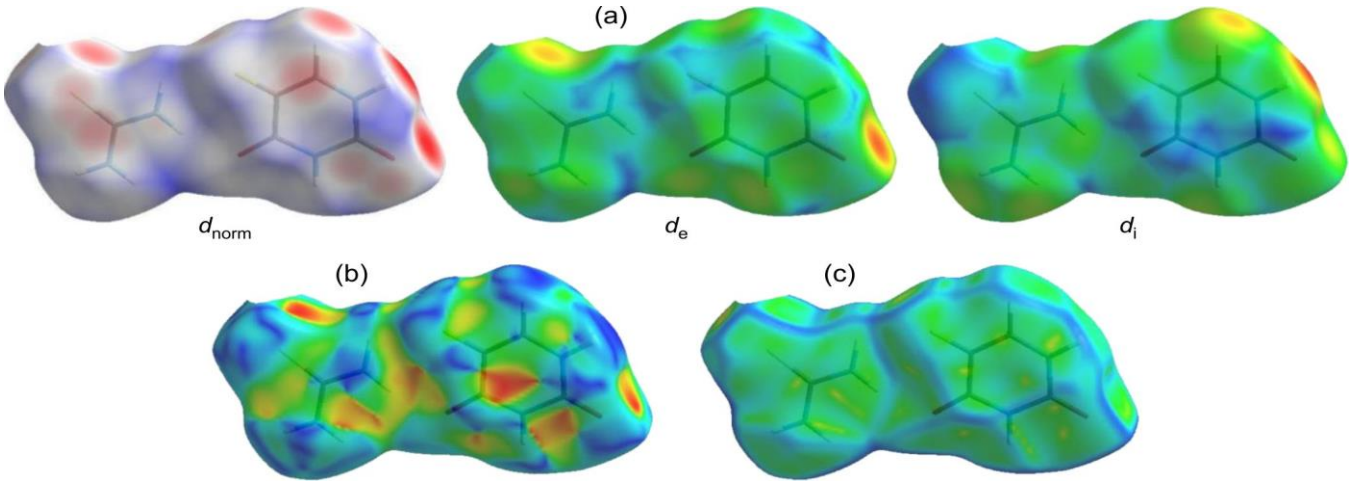


Fig. 3. (a) The d_{norm}, d_e and d_i in the Hirshfeld surface plot, (b) shape index and (c) curvedness for 5FUTU cocrystal

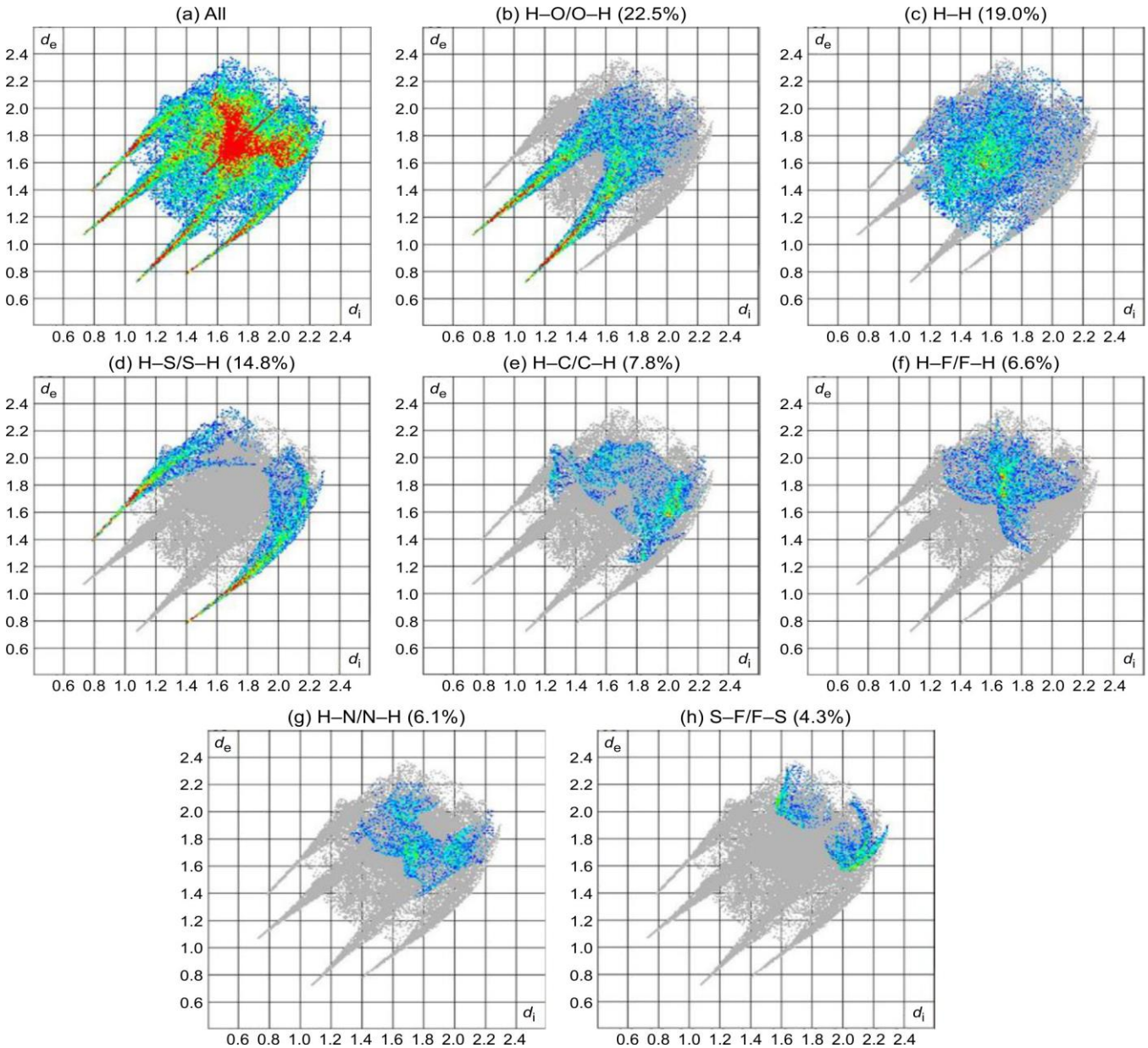


Fig. 4. Generated 2D fingerprint plot of 5FUTU cocrystal

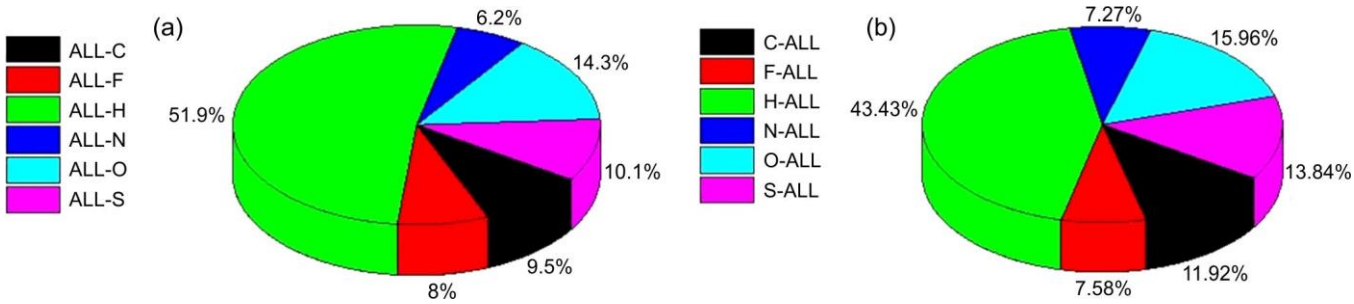


Fig. 5. (a) Percentage contribution of all atoms inside the Hirshfeld surface to an external atom and (b) percentage contribution of an internal atom to all surrounding external atoms

and 8.0%, respectively. The decomposed contact analysis shown in Fig. 5b provides further information on the interactions between individual atoms within the Hirshfeld surface and the surrounding atoms. H···ALL contacts again represent the largest contribution, at 43.43%, followed by F···ALL (15.96%), N···ALL (13.84%), O···ALL (11.92%), C···ALL (7.27%) and S···ALL (7.58%). These results demonstrate the involvement of several types of intermolecular contacts in the crystal packing of the 5FUTU cocrystal.

Vibrational spectral analysis: The 5FUTU cocrystal consists of 20 atoms and exhibits 54 normal vibrational modes. The optimized structure was used to calculate the vibrational frequencies and IR intensities, which are shown in Table-4. A scaling factor was applied to the calculated vibrational frequencies to account for anharmonicity and systematic errors associated with the DFT method. The empirical scaling factor for the 5FUTU cocrystal was determined using the following equation [25].

$$C = \frac{\sum(\nu_i \times \omega_i)}{\sum \omega_i^2}$$

where C is the empirical scaling factor equal to 1.0008; ν_i and ω_i are the detected and simulated fundamental incidences of FTIR. In Fig. 6, the recorded and theoretical FT-IR spectra are offered. The connection graph between the simulated and detected frequencies are shown in Fig. 7 and R^2 value 0.9996 shows there is good correlation between them.

C-H vibrations: The C–H stretching vibrations of pyrimidine derivatives are generally observed in the 3100-3000 cm^{-1} region and provide useful information for structural characterization [26]. For the 5FUTU cocrystal, the calculated vibrational mode assigned to C–H stretching occurs at 3225 cm^{-1} with 99% potential energy distribution (PED), while the corresponding experimental spectrum exhibits a prominent band at 3210 cm^{-1}. The difference of 15 cm^{-1} between the calculated and experimental frequencies may arise from the limitations of harmonic frequency calculations and the influence of the crystal environment. For benzene derivatives, in-plane C–H bending vibrations generally occur in the 1300-1000 cm^{-1} region, whereas out-of-plane bending vibrations are commonly found between 1000 and 750 cm^{-1} and within the broader 870-565 cm^{-1} range [27,28]. These vibrations are useful for distinguishing structural features and supporting spectral assignments [29]. The calculated in-plane bending modes occur at 1344, 1187 and 969 cm^{-1} with PED contri-

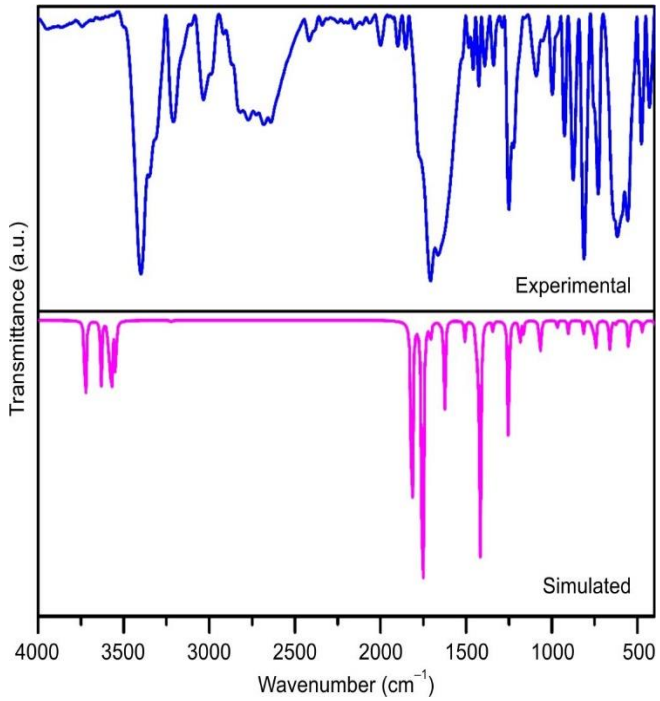


Fig. 6. Experimental and simulated FTIR spectra of 5FUTU cocrystal

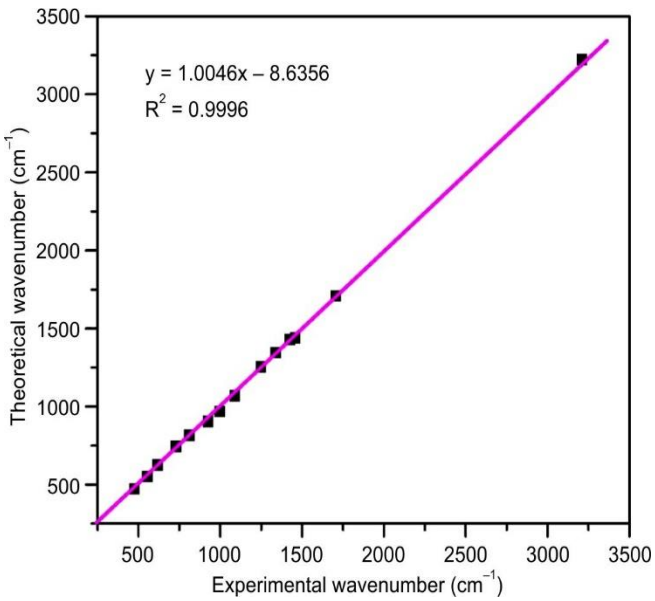


Fig. 7. Correlation graph between the experimental and simulated FTIR wavenumbers of 5FUTU

TABLE-4
COMPARISON OF THE EXPERIMENTAL FT-IR WAVENUMBERS (cm^{-1}) FOR 5-FLUOROURACIL THIOUREA COCRYSTAL AND THEORETICAL HARMONIC WAVENUMBERS (cm^{-1}) CALCULATED BY B3LYP/6-311++G(d,p) METHOD (Scale factor: 1.0008)

Mode	Experimental wavenumber (cm^{-1})	Calculated Wavenumber (cm^{-1})			Vibrational assignments (%PED)
		Calculated	Scaled	[a]I^{IR}	
1		3726.51	3729.49	139.14	ν_{as} NH_2(94)
2		3720.37	3723.34	103.56	ν_{as} NH_2(94)
3		3631.90	3634.80	140.08	ϕν NH(100)
4		3589.05	3591.92	82.13	ϕν NH(100)
5		3572.13	3574.98	264.74	νs NH_2(90)
6		3547.25	3550.08	143.22	νs NH_2(89)
7	3210 s	3222.73	3225.30	4.46	ϕ ν CH(99)
8		1816.98	1818.43	720.13	ϕ ν CO(75)
9		1754.10	1755.50	1085.5	ϕ ν CO(75)
10	1707 s	1708.70	1710.06	55.97	ϕ ν CC(67) + ϕ β CCH(11)
11		1649.67	1650.98	4.72	β HNH(90) sis
12		1626.14	1627.44	235.29	β HNH(72) sis
13		1507.76	1508.96	43.20	ϕ ν CN(23) + ϕ β CNH(34) + ϕ β CCN(10)
14	1458 m	1438.80	1439.95	98.58	ν CN(67) + β HNH(24) sis
15	1425 s	1427.80	1428.94	34.99	ϕ ν CN(10) + ϕ β CNC(15) + ϕ β CNH(24)
16		1418.71	1419.84	514.44	ν CN(16) + ν CS(12) + β CNH(45) + β NCN(12)
17		1413.07	1414.20	93.34	ϕ β CNH(53)
18	1340 m	1343.64	1344.71	22.70	ϕ ν CC(14) + ϕ β CCH(46)
19	1249 s	1252.84	1253.84	306.86	ϕ ν CN(27) + ϕ ν FC(41)
20		1186.29	1187.23	72.02	ϕ ν CN(64) + ϕ β CCH(14)
21		1164.83	1165.76	25.08	ϕ ν CN(26) + ϕ β CNH(19)
22	1089 m	1069.20	1070.05	82.17	ν CN(54) + β CNH(33)
23		1062.14	1062.98	24.52	ν CN(10) + β CNH(82)
24	997 s	968.07	968.84	15.07	ϕ ν CN(10) + ϕ β CNC(34) + ϕ β CNH(10) + ϕ β CCH(10)
25	925 s	903.67	904.39	27.35	τ CCCH(77) + τ CCNC(10)
26	812 vs	814.10	814.75	27.12	ϕ ν CN(10) + ϕ ν CF(20) + ϕ β CCN(21) + ϕ β CNC(13)
27		762.95	763.56	20.76	ν CS(67)
28		756.26	756.86	0.63	τ FCNC(10)
29		747.20	747.79	18.0	ϕ ν CN(29) + ϕ ν CNC(37)
30	729 vs	744.75	745.34	71.37	τ OCNC(71)
31		670.76	671.29	7.02	τ NCNH(26)
32		658.93	659.45	73.85	τ NCNH(84)
33		631.48	631.98	3.0	ϕ β CCO(27) + ϕ β NCO(26) + ϕ β FCC(26)
34	617 s	626.31	626.81	7.76	γ HNH(72) twist
35	555 s	551.43	551.87	59.93	τ CCNH(94)
36		542.61	543.04	15.78	ϕ ν CN(27) + ϕ β CNC(39) + ϕ β NCN(13)
37		490.49	490.88	2.24	τ NCNH(33)
38	476 vs	472.28	472.65	22.49	ν CS(13) + β NCN(73)
39		458.78	459.14	8.52	ϕ β NCO(13) + ϕ β CCN(10) + ϕ β CNC(26) + ϕ β NCN(17)
40		399.46	399.77	0.02	β SCN(89)
41		393.44	393.75	16.71	ϕ ν CN(10) + ϕ β CCO(17) + ϕ ν NCO(33)
42		380.70	381.00	8.7	τ CCCH(19) + τ CNCC(29) + τ FCCN(29)
43		345.08	345.35	41.77	τ CNCC(28) + τ CNCN(17)
44		320.24	320.49	193.41	τ NCNH(46)
45		312.32	312.56	1.21	ϕ β CCO(20) + ϕ ν CCN(15) + ϕ ν FCC(43)
46		153.82	153.94	1.47	τ CNCN(86)
47		136.00	136.10	15.44	τ NCNH(56)
48		114.30	114.39	7.94	τ CCNC(24) + τ CNCN(70)
49		77.75	77.81	5.09	ν OH(89)
50		71.07	71.12	3.66	γ NHO(79)
51		26.81	26.831448	2.83	τ NCNH(27)
52		18.63	18.644904	0.03	τ NCNH(22)
53		17.60	17.61408	0.82	β CCO(91)
54		11.34	11.349072	0.03	τ NCNH(10)

w: weak; vs: very strong; m: medium; ν: Stretching; ν_s: symmetric stretching; ν_{as}: asymmetric stretching; β: in plane bending; γ: out-of-plane bending; τ: torsion; ϕ: ring

butions of 46, 14 and 10%, respectively. Experimentally, the prominent and medium-intensity bands are observed at 997 and 1340 cm^{-1}, respectively. The calculated torsional modes appear at 381 and 904 cm^{-1} with PED contributions of 19 and 77%, respectively. The experimental band at 997 cm^{-1} lies near the calculated 904 cm^{-1} mode, although this correspondence requires confirmation from the normal-mode displacement and PED analysis. The calculated spectra are in good agreement with the experimental results and reported vibrational assignments [30,31].

NH_2 vibrations: The NH_2 group exhibits characteristic scissoring, rocking, wagging, twisting and symmetric and asymmetric stretching vibrations [32]. For the 5FUTU cocrystal, the calculated asymmetric stretching modes occur at 3729 and 3723 cm^{-1}, each with a PED contribution of 94%. The symmetric stretching modes are calculated at 3575 and 3550 cm^{-1} with 100% PED contributions. The NH_2 scissoring modes appear at 1651, 1627 and 1438 cm^{-1} with corresponding PED contributions of 90, 70 and 24%. The twisting vibrations are calculated at 320 and 136 cm^{-1} with PED contributions of 46 and 56%, while the wagging modes occur at 627 and 490 cm^{-1} with contributions of 33 and 72%, respectively. These assignments were compared with previously reported data for related compounds [32,33].

N-H vibrations: The N–H stretching and bending frequencies are sensitive to the molecular environment and the nature of hydrogen bonding. The N–H stretching vibrations in heterocyclic compounds are commonly observed in the 3200-3500 cm^{-1} region [34]. For the pyrimidine ring in 5FUTU, DFT calculations assign two predominantly pure N–H stretching modes at 3635 and 3569 cm^{-1}, each with 100% PED contribution. The calculated N–H in-plane bending modes occur at 1509, 1429, 1420, 1166, 1070, 1063 and 969 cm^{-1} with PED contributions of 34, 24, 45, 19, 33, 82 and 10%, respectively. The experimental FTIR spectrum exhibits a prominent band at 1425 cm^{-1}, together with bands at 1340, 1089 and 997 cm^{-1}. The calculated N–H out-of-plane bending modes occur at 671, 659, 552 and 491 cm^{-1}, with PED contributions of 26, 84, 94 and 33%, respectively. A strong experimental band at 555 cm^{-1} is assigned to N–H out-of-plane bending. These assignments provide a basis for comparing the calculated vibrational modes with the experimental spectrum and previously reported data for analogous compounds. The changes in the N–H and NH_2 stretching frequencies may be associated with altered hydrogen-bonding environments in the cocrystal.

C-F modes: The C–F stretching vibrations are generally observed in the 1450-1000 cm^{-1} region and often give rise to intense infrared absorption bands [35]. In 5FUTU cocrystal, the calculated C–F stretching mode occurs at 1254 cm^{-1} with a PED contribution of 41%. The experimental FTIR spectrum exhibits a strong band at 1249 cm^{-1}, in close agreement with the calculated frequency. This assignment is consistent with previously reported data [36]. The calculated C–F in-plane bending modes occur at 632 and 313 cm^{-1}, with PED contributions of 26 and 43%, respectively. The out-of-plane bending modes are calculated at 757 and 381 cm^{-1} with corresponding PED contributions of 10 and 29%. These assignments are supported by literature data for related compounds [37,38].

C=O vibrations: The carbonyl (C=O) stretching vibration is a characteristic feature of infrared spectra and generally appears in the 1800-1650 cm^{-1} region for many carbonyl containing compounds [39]. The C=O bond comprises a σ-bond and a π-bond formed by orbital overlap between carbon and oxygen. In 5FUTU cocrystal, the two carbonyl stretching modes are calculated at 1818 and 1756 cm^{-1}, each with a PED contribution of 75%. The calculated frequencies lie within the broader carbonyl stretching region, although their positions should be interpreted in relation to the molecular environment and hydrogen bonding. The in-plane bending modes associated with the C=O groups are calculated at 632, 459, 394 and 312 cm^{-1} with PED contributions of 53, 13, 50 and 20%, respectively. The mode calculated at 745 cm^{-1} is assigned predominantly to OCNC torsion with a PED contribution of 71%.

C-C, C-N and C-S vibrations: The assignment of C–N and C–C stretching vibrations can be challenging due to the overlap of several vibrational modes in the same spectral region. C–N stretching bands commonly occur between 1380 and 1100 cm^{-1}, although their positions and intensities depend on conjugation, hydrogen bonding and the surrounding molecular environment [40]. For the pyrimidine ring of 5FU in the 5FUTU cocrystal, DFT/B3LYP calculations yielded C–N stretching modes at 1509, 1429, 1254, 1187, 1166, 968, 815, 748, 543, and 393 cm^{-1}, with corresponding PED contributions of 23, 10, 27, 64, 26, 10, 10, 29, 27 and 10%, respectively. The C–N stretching modes associated with the thiourea moiety were calculated at 1490, 1420 and 1063 cm^{-1} with PED contributions of 67, 10 and 10%. The experimental FTIR spectrum exhibits prominent bands at 1425, 1249, 997 and 812 cm^{-1}, while the band at 1089 cm^{-1} is assigned to C–N stretching in the thiourea moiety. The calculated C–N in-plane bending modes occur at 1429, 1420, 968 and 748 cm^{-1} with the corresponding PED contributions requiring verification against the normal-mode analysis. Experimentally, the bands at 1425, 997 and 812 cm^{-1} were associated with these vibrations. In benzene derivatives, C–C stretching vibrations commonly occur within the 1650-1100 cm^{-1} region. For 5FUTU, the calculated C–C stretching modes include contributions at 1710 and 1344 cm^{-1}, with PED values of 67 and 14%, respectively. The experimental spectrum exhibits a very strong band at 812 cm^{-1} and a moderately intense band at 1340 cm^{-1}; these assignments should be considered alongside other possible vibrational contributions in the same region. The calculated C–C in-plane bending modes occur at 1509, 815 and 459 cm^{-1} with PED contributions of 10, 21 and 10%, respectively. The pyrimidine-ring torsional modes of the 5-fluorouracil moiety are calculated below 381 cm^{-1}, with PED contributions ranging from 10 to 86%. For the thiourea moiety, the C–S stretching and in-plane bending modes were calculated at 764 and 400 cm^{-1} with PED contributions of 67 and 89%, respectively. The thiourea moiety contains a single C–S bond, which make the assignment of its associated vibrational modes particularly relevant to the interpretation of the calculated spectrum.

Natural bond orbital (NBO) analysis: The NBO analysis was performed using the NBO program implemented in Gaussian at the DFT/B3LYP level to examine the electron distribution and donor–acceptor interactions in the 5FUTU

cocrystal [41]. Second-order perturbation theory was used to estimate the stabilization energies associated with interactions between occupied donor orbitals and unoccupied acceptor orbitals [42-44]. These interactions describe electron delocalization within the molecular units and provide insight into their electronic stabilization. The donor–acceptor interactions and corresponding stabilization energies are listed in Table-5. Electron donation into antibonding orbitals increases their occupancy and may weaken the associated bonds. In thiourea (molecular unit 1), the σ(C1–S8)→σ*(C1–S8) interaction has a stabilization energy of 6.47 kcal/mol, while π(C1–S8)→σ*(N2–H3) and π(C1–S8)→σ*(N5–H6) interactions contribute 3.30 and 3.32 kcal/mol, respectively. Lone-pair donation from LP(2) of S8 to σ*(C1–N2) and σ*(C1–N5) gives stabilization energies of 10.87 and 10.96 kcal/mol, respectively. The reported LP(1)(N2, N5)→σ*(C1–S8) interactions have higher stabilization energies of 72.71 and 71.08 kcal/mol, respectively. In the 5-fluorouracil unit (molecular unit 2), the π(C10–C12)→σ*(C13–O20) interaction has a stabilization energy of 21.99 kcal/mol. Other reported donor-acceptor interactions involving the lone pairs of F14, N15, N17, O19 and O20 and the antibonding orbitals of the C–C, C–O, C–N and related bonds have stabilization energies ranging from 18.20 to 54.93 kcal/mol. These interactions contribute to electron delocalization within the 5-FU unit. The analysis further identified weaker interactions between the two mole-cular units, involving LP(1) or LP(2) of O20 and the σ*(N2–H3) and σ*(N5–H6) orbitals, with stabilization energies of 1.32, 1.94, and 2.30 kcal/mol. These donor-acceptor interactions are consistent with a contribution from hydrogen bonding between thiourea and 5-fluorouracil in the cocrystal. The NBO results distinguish the stronger intramolecular electronic interactions from the weaker interactions between the two molecular units.

UV-Vis spectra: UV-visible spectroscopy was used to investigate the electronic transitions of 5FUTU in water. Fig. 8 shows the experimental and TD-DFT-calculated UV-visible spectra obtained using the optimized molecular structure. The calculated absorption parameters are listed in Table-6. The TD-DFT calculation predicted an absorption maximum at 303 nm, which correspond to an excitation energy of 4.096 eV and arising predominantly from the HOMO-1→LUMO transition (100%). The experimental spectrum showed an absorption peak at 270 nm. The calculated transition was assigned to a π→π* excitation, which is associated with electronic delocalization within the pyrimidine ring system [45].

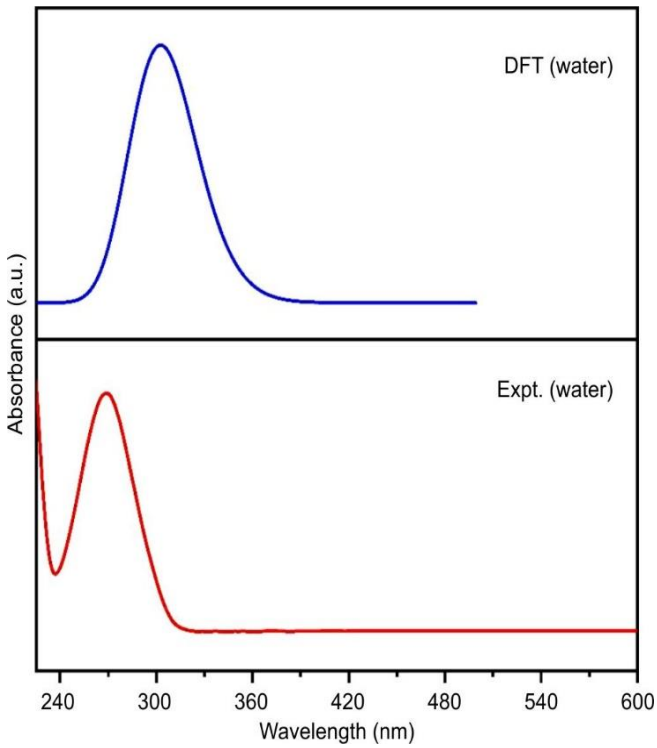


Fig. 8. Experimental and simulated UV-Vis absorbance spectra of 5FUTU cocrystal

Topology analyses

ELF and LOL analysis: The electron localization function (ELF) and localized orbital locator (LOL) were used to examine the distribution and localization of electrons in the 5FUTU cocrystal using Multiwfn [46,47]. Both descriptors are related to the kinetic-energy density, but they differ in their theoretical basis and provide information on electron localization [46]. Fig. 9 presents the colour maps and corresponding projections of ELF and LOL for the 5FUTU molecular units. ELF, denoted by τ(r), ranges from 0 to 1, with higher values representing strong electron localization in regions associated with covalent bonds, lone pairs and atomic shells. The values between 0.5 and 1 generally correspond to localized electron regions, whereas values below 0.5 are associated with higher electron delocalization [46]. LOL, denoted by η(r), provides a view of orbital localization, with values above 0.5 generally indicating localized regions [48]. In Fig. 9a, the higher ELF regions around hydrogen atoms are attributed to localized electron density. The blue regions near selected carbon atoms represent areas of comparatively lower electron localization. In the LOL map (Fig. 9b), the white regions around hydrogen nuclei indicate values exceeding the upper limit of the displayed colour scale (0.80). Blue rings around the carbon, nitrogen, and sulphur nuclei represent regions of reduced electron density between the inner and valence shells. The red regions between nitrogen and hydrogen atoms indicate strong electron localization in the corresponding bonding regions. Compared with ELF, LOL provides a sharper and more distinct representation of electron localization.

Molecular electrostatic potential (MEP) study: The MEP analysis illustrates the charge distribution and relative polarity of a molecule [49,50]. The three-dimensional MEP surface identifies electron-rich and electron-deficient regions, helping locate potential sites for electrophilic and nucleophilic interactions.

$$V(r) = \sum_{A} \frac{Z_A}{|R_A - r|} - \int \frac{\rho(r)\,dr'}{|r' - r'|}$$

where ρ(r) represents electron density and Z_A represents the charge on nucleus A, positioned at R_A [51]. The molecular electrostatic potential (MEP) surface of the 5FUTU cocrystal is presented in Fig. 10a. The electrostatic potential (V(r)) represents the combined contributions of the nuclei and electrons at a given point and provides insight into molecular polarity, reactivity and intermolecular interactions. In the MEP

TABLE-5
KEY DONOR-ACCEPTOR INTERACTIONS AND THE SECOND ORDER PERTURBATION ENERGIES OF CO-CRYSTAL 5-FLUOROURACIL THIOUREA CALCULATED USING THE B3LYP/6-311++G(d,p) LEVEL OF THEORY

Molecular unit 1 (Thiourea moiety)								
Bond type	Donor (i)	Occupancy (Ed/e)	Bond type	Acceptor (j) (Ed/e)	Occupancy	$E^{(2)}$	E(j) – E(i)	F(i,j)
σ	C1-N2	1.99321	σ*	N5-H7	0.00738	2.14	1.28	0.047
σ	C1-N5	1.99319	σ*	N2-H4	0.00748	2.17	1.28	0.047
σ	C1-S8	1.99009	σ*	C1-S8	0.50069	6.47	0.2	0.037
π	C1-S8	1.97858	σ*	N2-H3	0.02222	3.3	1.1	0.054
π	C1-S8	1.97858	σ*	N5-H6	0.01872	3.32	1.1	0.054
σ	N2-H3	1.98648	π*	C1-S8	0.01530	5.07	0.98	0.063
σ	N2-H4	1.98865	σ*	C1-N5	0.05015	4.37	1.13	0.063
σ	N5-H6	1.98666	π*	C1-S8	0.01530	5	0.98	0.062
σ	N5-H7	1.98885	σ*	C1-N2	0.04959	4.3	1.13	0.063
LP(1)	N2	1.73841	σ*	C1-S8	0.50069	72.71	0.21	0.117
LP(1)	N5	1.74388	σ*	C1-S8	0.50069	71.08	0.21	0.116
LP(1)	S8	1.98471	σ*	C1-N2	0.04959	3.28	1.14	0.055
LP(1)	S8	1.98471	σ*	C1-N5	0.05015	3.24	1.14	0.055
LP(2)	S8	1.89335	σ*	C1-N2	0.04959	10.87	0.65	0.076
LP(2)	S8	1.89335	σ*	C1-N5	0.05015	10.96	0.64	0.076
Molecular unit 2 (5-Flurouracil moiety)								
Bond type	Donor (i)	Occupancy (Ed/e)	Bond type	Acceptor (j)	Occupancy (Ed/e)	$E^{(2)}$	E(j) – E(i)	F(i,j)
π	C9-O19	1.99303	π*	C9-O19	0.34677	2.14	0.38	0.028
σ	C10-H11	1.97787	σ*	C9-N15	0.08455	4.02	0.97	0.057
σ	C10-H11	1.97787	σ*	C12-C13	0.07255	3.75	1	0.056
σ	C10-C12	1.98392	σ*	C12-C13	0.07255	2.28	1.22	0.048
σ	C10-C12	1.98392	σ*	C13-O20	0.01045	2.18	1.37	0.049
σ	C10-C12	1.98392	σ*	N15-H16	0.01197	2.36	1.17	0.047
π	C10-C12	1.85325	π*	C13-O20	0.33617	21.99	0.31	0.078
σ	C10-N15	1.98502	σ*	C9-O19	0.00902	2.2	1.47	0.051
σ	C10-N15	1.98502	σ*	C12-F14	0.01865	3.32	1.13	0.055
σ	C12-C13	1.97815	σ*	C10-H11	0.01093	2.46	1.1	0.047
σ	C12-C13	1.97815	σ*	C10-C12	0.02116	3.19	1.29	0.057
σ	C12-C13	1.97815	σ*	N17-H18	0.01314	2.62	1.09	0.048
σ	C13-N17	1.98736	σ*	C12-F14	0.01865	2.23	1.11	0.044
π	C13-O20	1.98360	π*	C10-C12	0.22761	4.58	0.39	0.04
σ	N15-H16	1.98571	σ*	C9-N17	0.08491	2.98	1.09	0.052
σ	N15-H16	1.98571	σ*	C10-C12	0.02116	2.04	1.28	0.046
σ	N17-H18	1.98413	σ*	C9-N15	0.08455	3.24	1.07	0.053
σ	N17-H18	1.98413	σ*	C12-C13	0.07255	2.29	1.11	0.046
LP(2)	F14	1.96427	σ*	C10-C12	0.02116	6.29	1.01	0.071
LP(2)	F14	1.96427	σ*	C12-C13	0.07255	7.32	0.85	0.071
LP(3)	F14	1.93253	π*	C10-C12	0.22761	19.59	0.42	0.085
LP(1)	N15	1.65218	π*	C9-O19	0.34677	52.69	0.29	0.111
LP(1)	N15	1.65218	π*	C10-C12	0.22761	40.9	0.29	0.101
LP(1)	N17	1.64403	π*	C9-O19	0.34677	53.78	0.28	0.111
LP(1)	N17	1.64403	π*	C13-O20	0.33617	54.93	0.28	0.111
LP(2)	O19	1.83431	σ*	C9-N15	0.08455	26.74	0.65	0.12
LP(2)	O19	1.83431	σ*	C9-N17	0.08491	26.74	0.65	0.12
LP(1)	O20	1.97510	σ*	C12-C13	0.07255	2.01	1.14	0.043
LP(2)	O20	1.86247	σ*	C12-C13	0.07255	18.2	0.7	0.103
LP(2)	O20	1.86247	σ*	C13-N17	0.08092	26.7	0.67	0.121
Molecular unit 2 to 1 (Intermolecular interaction)								
Bond type	Donor (i)	Occupancy (Ed/e)	Bond type	Occupancy (Ed/e)	Occupancy	$E^{(2)}$	E(j) – E(i)	F(i,j)
LP(1)	O20	1.97510	σ*	N2-H3	0.02222	1.32	1.18	0.035
LP(1)	O20	1.97510	σ*	N5-H6	0.01872	1.94	1.18	0.043
LP(2)	O20	1.86247	σ*	N2-H3	0.02222	2.3	0.75	0.038

[a]$E^{(2)}$ means energy of hyperconjugative interactions; [b]Energy difference between donor and acceptor i and j NBO orbitals; [c]F(i,j) is the Fock matrix element between i and j NBO orbitals.

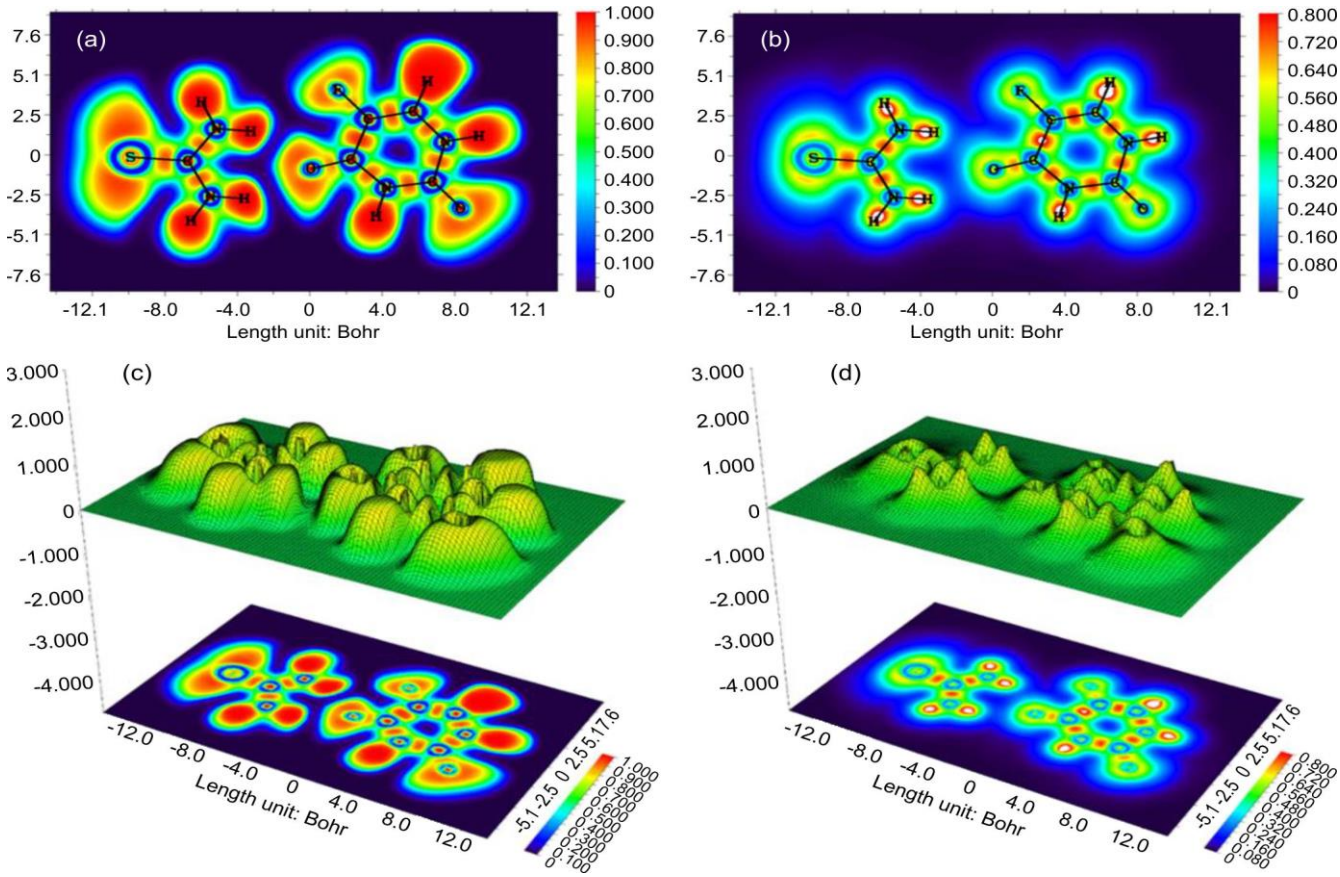


Fig. 9. (a) ELF (b) ELF (c) LOL and (d) LOL maps of 5FUTU

TABLE-6
CALCULATED AND OBSERVED UV-VIS SPECTRAL PARAMETERS AND THE CORRESPONDING ASSIGNMENT OF ELECTRONIC TRANSITION OF 5FUTU COCRYSTAL

Contribution of orbitals	Theoretical			Experimental		Assignments
	λ (nm)	E (eV)	f	λ (nm)	E (eV)	
H-1→ L	277	4.476	0.95	269	4.609	π → π*

map, red indicates the most negative potential, followed by orange and yellow, while green represents near-neutral potential and blue denotes the most positive potential. The negative regions are electron-rich and may attract protons, whereas positive regions are electron-deficient and may repel them. Red regions are associated with potential sites for electrophilic attack, while blue regions may favour nucleophilic attack. The orange region near the S8 atom and the blue region around the three hydrogen atoms of the pyrimidine ring represent distinct electrostatic environments. Fig. 10b presents the ESP isosurfaces, while Fig. 10c shows the electron-density distribution and Fig. 10d displays the ESP profile. These maps help identify chemically reactive sites and assess possible intermolecular interactions including hydrogen bonding based on the charge distribution of the molecule [49,50].

Non-covalent interaction reduced density gradient analysis: The non-covalent interaction (NCI) method is widely used to visualize the intermolecular interactions including hydrogen bonds, van der Waals contacts and steric repulsion, through the reduced density gradient (RDG) [52], defined by the following equation.:

$$s = \frac{1}{\left(2(3\pi^2)^{1/3}\right)} \frac{|\Delta\rho|}{\rho^{4/3}}$$

The reduced density gradient (RDG) is used to characterize non-covalent interactions based on the sign of the second eigen value of the electron-density Hessian (Sign(λ2)ρ). Negative values indicate attractive interactions, values near zero are associated with van der Waals interactions and positive values indicate steric repulsion [53-55]. In the NCI isosurfaces, blue, green and red represent strong attractive interactions, weak van der Waals interactions and steric repulsion, respectively. The two-dimensional RDG plot provides information about these interactions.

Fig. 11 presents the three-dimensional RDG isosurfaces and two-dimensional scatter plot for 5FUTU. The small red spike near 0.02 a.u. indicates steric repulsion, while the green spikes at approximately -0.0110 and -0.0115 a.u. correspond to weak van der Waals interactions. Blue regions between

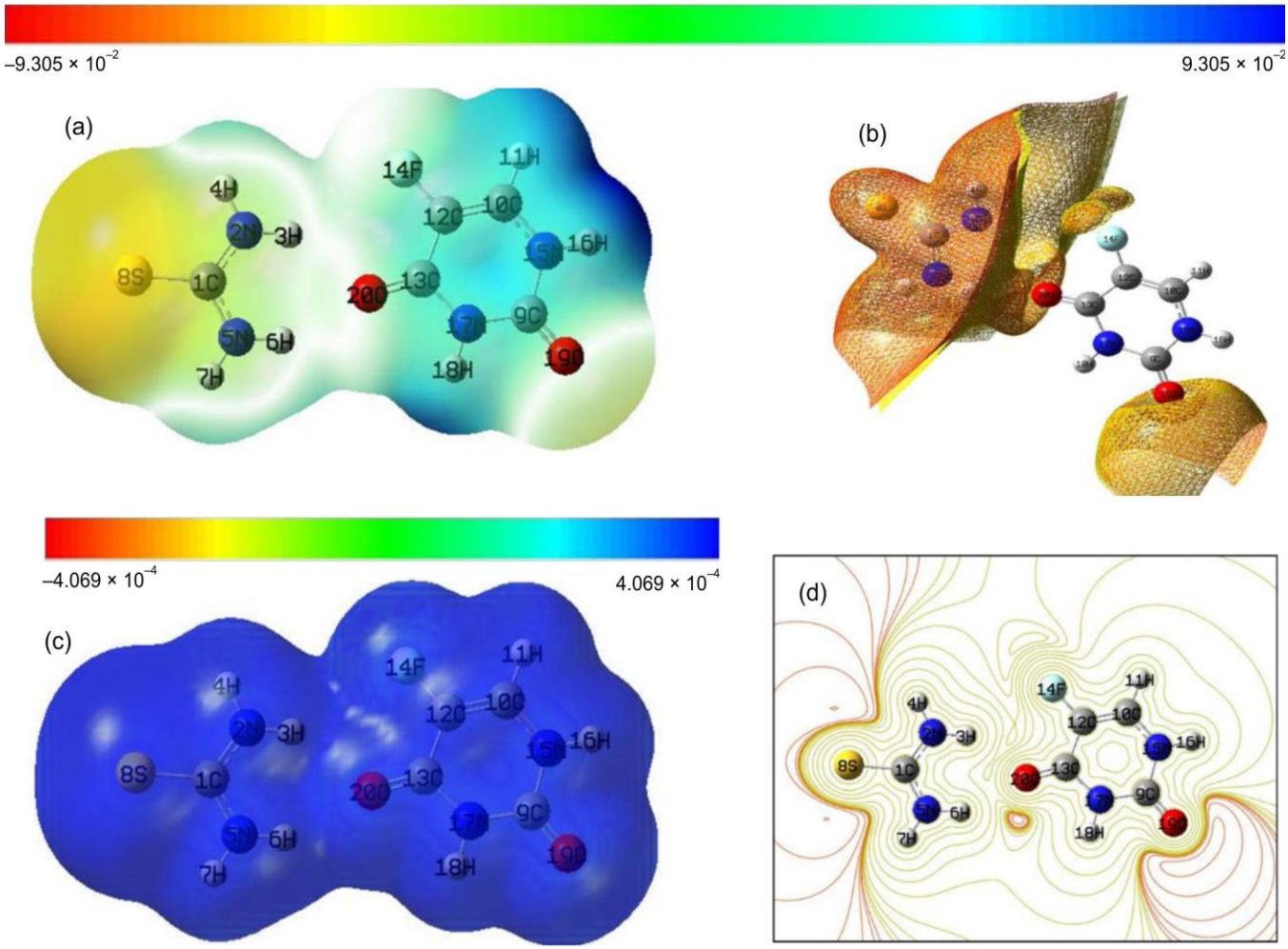


Fig. 10. (a) Molecular electrostatic potentials, (b) Plot of ESP isosurface, (c) Mapping of total density and (d) ESP 2D contours array plot for 5FUTU cocrystal

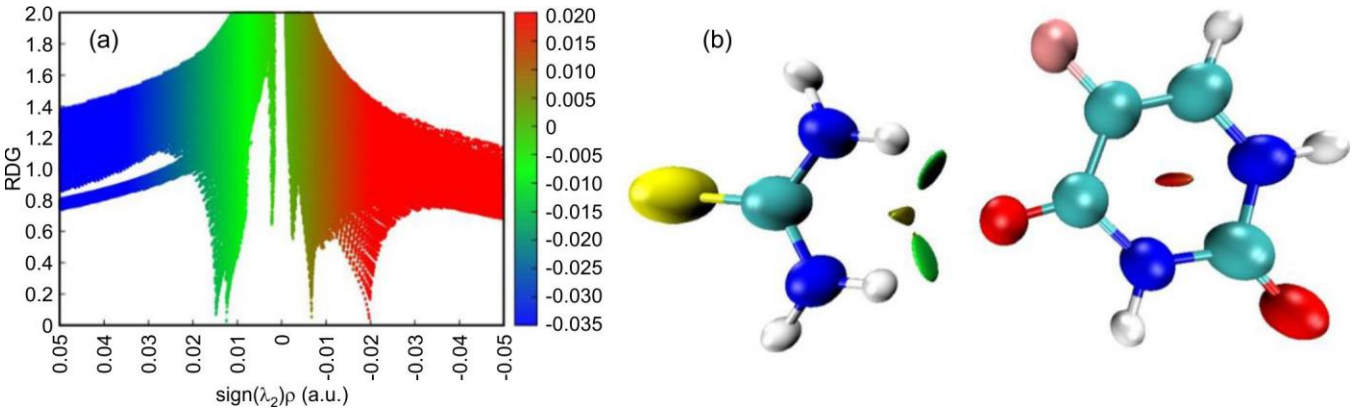


Fig. 11. 2D Scatter and iso-surface density plots of 5FUTU cocrystal

-0.025 and -0.05 a.u. indicate stronger attractive interactions including the proposed N–H···O and N–H···S hydrogen bonds. The interactions involving LP(1) O20···N2–H3, LP(2) O20···N2–H3, and LP(1) O20···N5–H6 further describe the reported hydrogen-bonding contacts. Green patches between hydrogen atoms indicate weak H···H contacts. Red isosurfaces within the ring region are associated with steric effects. The RDG results support the presence of attractive and repulsive non-covalent interactions in 5FUTU, consistent with its structural features and Hirshfeld surface (HS) analysis.

Frontier molecular orbital (FMO): The FMOs of the 5FUTU cocrystal were analyzed using DFT/B3LYP with the 6-311++G(d,p) basis set. The system contains 106 electrons distributed across 53 doubly occupied molecular orbitals. Fig. 12 presents the HOMO and LUMO distributions and their energy levels. The HOMO is mainly localized around the N–H

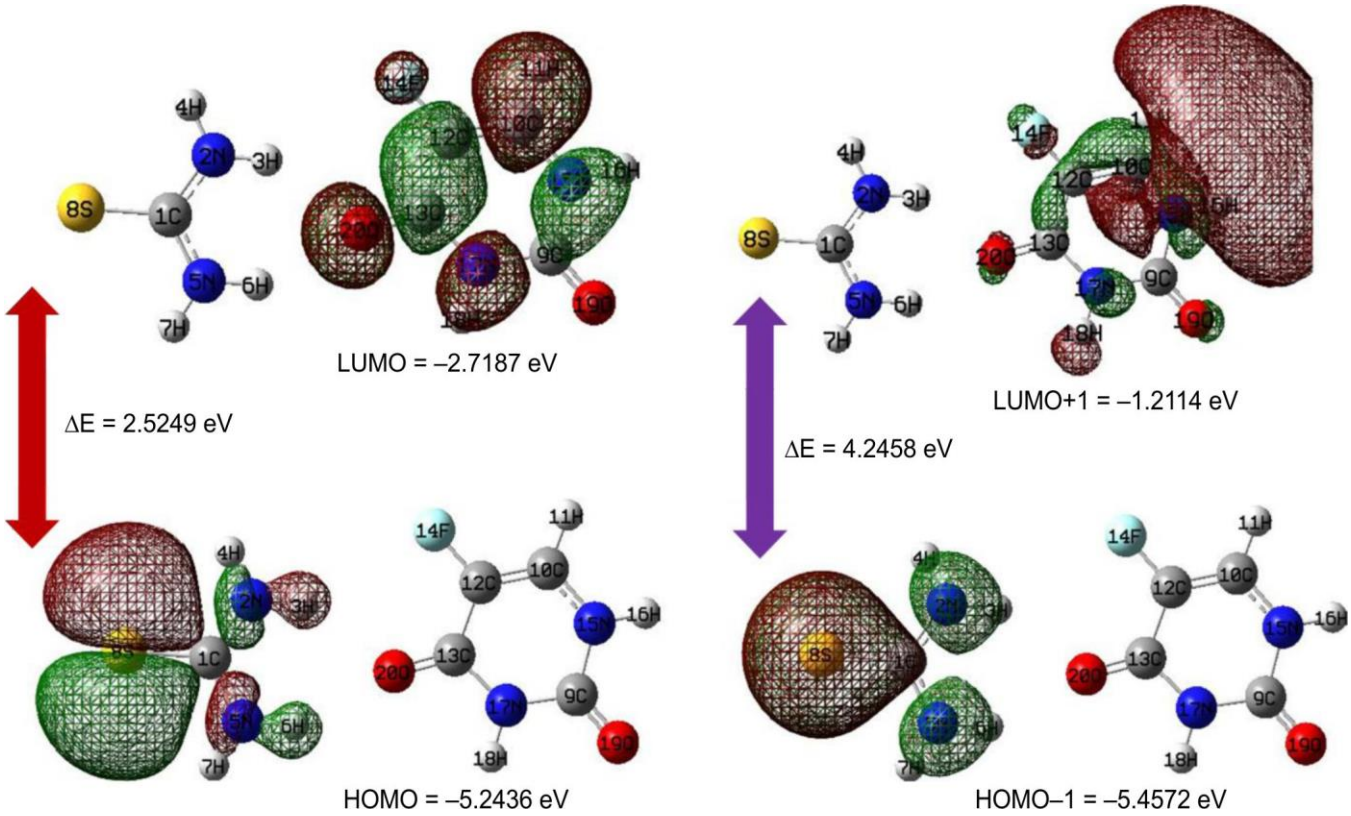


Fig. 12. Frontier molecular orbitals (FMOs) of 5FUTU cocrystal with HOMO and LUMO orbitals

and C–S bonds of the thiourea moiety, whereas the LUMO is distributed across the C–C, C–N, C–H, and N–H bonding regions of the 5-fluorouracil moiety. This distribution suggests possible electronic redistribution between the two molecular components upon excitation.

The calculated HOMO and LUMO energies are -5.2436 and -2.7187 eV, respectively, giving an energy gap ($\Delta E = E_{LUMO} - E_{HOMO}$) of 2.5249 eV. A smaller HOMO–LUMO gap generally indicates that electronic excitation may occur more readily and can be associated with increased chemical reactivity and lower chemical hardness. Global reactivity descriptors were calculated using Koopmans' approximation. The electron affinity (A) is 2.7187 eV and the ionization potential (I) is 5.2436 eV. The chemical potential (μ), chemical hardness (η), electrophilicity index (ω) and softness (S) are -3.9812 eV, 1.2625 eV, 6.2772 eV and 0.7921 eV^{-1}, respectively. The electronegativity (χ) is 3.9812 eV, calculated as ((I+A)/2). These descriptors provide information about the electronic properties and potential reactivity of the cocrystal. The HOMO and LUMO contain contributions from σ- and σ*-type orbitals.

The density of states (DOS) spectrum (Fig. 13) describes the distribution of molecular orbital states over the investigated energy range. The occupied states are assigned to the -20 to -5 eV region, while the unoccupied states lie between -5 and 0 eV. Large DOS intensity at a given energy indicates a higher concentration of molecular states within that region.

Mulliken atomic charges: Mulliken population analysis was performed at the B3LYP/6-311++G(d,p) level to examine the atomic charge distribution in the 5FUTU cocrystal. The

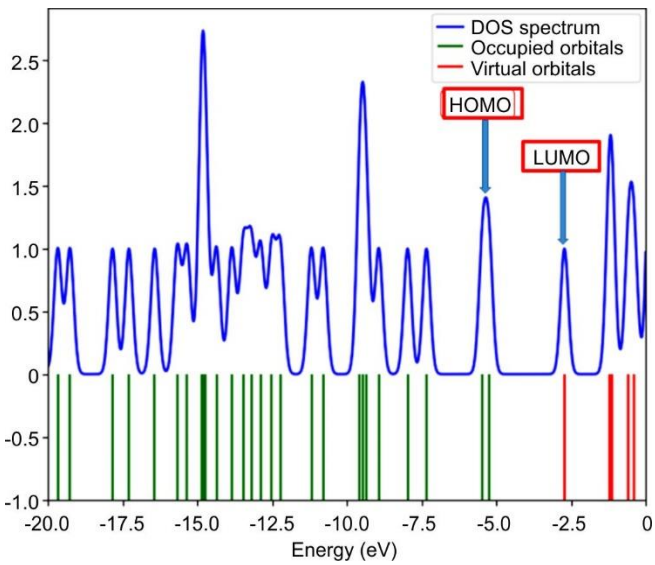


Fig. 13. Density of states (DOS) spectrum of 5FUTU cocrystal

calculated charges are listed in Table-7 and their distribution is shown in Fig. 14. All hydrogen atoms carry positive partial charges. The highest values occur at H3 (+0.397133e), H6 (+0.354078e), H16 (+0.365854e) and H18 (+0.369170e), mainly due to their bonding with electronegative nitrogen atoms in the thiourea and 5-fluorouracil moieties. Carbon atoms C10, C9 and C13 are positively charged, whereas C12 and the sulfur atom carry negative charges. The nitrogen atoms N2, N5, N15, and N17 also exhibit negative partial charges and may act as electron-rich sites. This charge distribution is

TABLE-7
MULLIKEN ATOMIC CHARGE OF ATOMS IN 5FUTU COCRYSTAL CALCULATED BY B3LYP/6-311++G(d,p) METHOD

Atom	Charge/e	Atom	Charge/e	Atom	Charge/e	Atom	Charge/e
C1	0.032906	H6	0.353078	H11	0.214472	H16	0.365854
N2	-0.31221	H7	0.274604	C12	-0.04207	N17	-0.39561
H3	0.397133	S8	-0.65707	C13	0.195838	H18	0.36917
H4	0.261848	C9	0.323376	F14	-0.17636	O19	-0.30951
N5	-0.33261	C10	0.183971	N15	-0.37828	O20	-0.36853

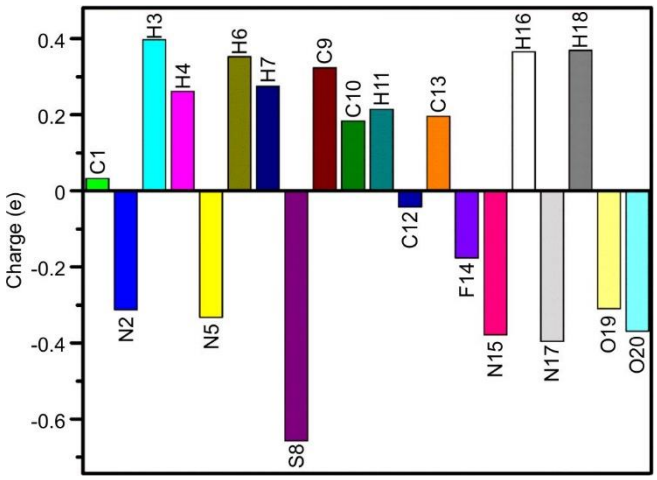


Fig. 14. Mulliken atomic charge of atoms in 5FUTU cocrystal

consistent with the potential formation of intermolecular and intramolecular N–H···O hydrogen bonds, although confirmation requires structural and interaction analyses.

Fukui functions analysis: Global reactivity descriptors include electronegativity (χ), chemical hardness (η) and softness (S). The Fukui function is a local reactivity descriptor that describes changes in electron density with respect to electron number while keeping the nuclear positions fixed [56]. It helps identify atomic sites susceptible to electrophilic or nucleophilic attack. The Fukui function (f_j^+) describes the response of atom (j) to electron addition and identifies sites prone to nucleophilic attack, whereas (f_j^-) describes electron removal and identifies sites susceptible to electrophilic attack. The condensed Fukui functions assign a numerical reactivity index to each atom, which allow the likely reactive sites in the molecular structure to be identified. The expressions for (f_j^+) and (f_j^-) are given below:

$$f_j^- = q_j(N) - q_j(N-1)$$

$$f_j^+ = q_j(N+1) - q_j(N)$$

$$f_j^0 = \frac{1}{2}\left[q_j(N+1) - q_j(N-1)\right]$$

where (N), (N – 1) and (N + 1) are the total electrons present in the neutral, cation and anion situations of the explored molecule, correspondingly and q_j is the Mulliken charge values at the j^{th} atomic spot. The difference amid an electrophilic and a nucleophilic Fukui method was acknowledged as the condensed dual descriptor Δf(r) that might be stated in this manner: $\Delta f(r) = f_j^+ - f_j^-$ [57]. The dual descriptors in addition to condensed Fukui method derived from the Mulliken charge distribution are revealed in Table-8. The sign of the Fukui function difference (Δf) helps identify reactive sites. Positive values indicate a better tendency toward electrophilic attack, whereas negative values suggest the susceptibility to nucleo-

TABLE-8
LIST OF LOCAL REACTIVITY DESCRIPTORS VALUES OF 5FUTU COCRYSTAL MOLECULE CALCULATED BY DFT

Atoms	q_j	q_j (N+1)	q_j (N–1)	f_j^+	f_j^-	f_j^0	Δf(r)
C1	0.032906	0.311898	0.135285	0.278992	-0.10238	0.088307	0.38137
N2	-0.31221	-0.308370	-0.31853	0.003837	0.006321	0.005079	-0.00248
H3	0.397133	0.454402	0.446072	0.057269	-0.048940	0.004165	0.10620
H4	0.261848	0.295163	0.249823	0.033315	0.012025	0.022670	0.02129
N5	-0.33261	-0.326040	-0.327790	0.006572	-0.004820	0.000876	0.01139
H6	0.353078	0.328268	0.292731	-0.024810	0.060347	0.017769	-0.08516
H7	0.274604	0.307096	0.248607	0.032492	0.025997	0.029245	0.00649
S8	-0.65707	-0.166020	-0.740900	0.491046	0.083834	0.287440	0.40721
C9	0.323376	0.314730	0.324361	-0.008650	-0.000990	-0.004820	-0.00766
C10	0.183971	0.232082	-0.036770	0.048111	0.220743	0.134427	-0.17263
H11	0.214472	0.236444	0.120168	0.021972	0.094304	0.058138	-0.07233
C12	-0.04207	-0.027620	-0.103390	0.014452	0.061316	0.037884	-0.04686
C13	0.195838	0.185003	0.112717	-0.010840	0.083121	0.036143	-0.09396
F14	-0.17636	-0.186250	-0.248890	-0.009890	0.072532	0.031320	-0.08243
N15	-0.37828	-0.354840	-0.354420	0.023438	-0.023860	-0.000210	0.04729
H16	0.365854	0.382295	0.302137	0.016441	0.063717	0.040079	-0.04728
N17	-0.39561	-0.409370	-0.444180	-0.013760	0.048570	0.017404	-0.06233
H18	0.36917	0.375129	0.304217	0.005959	0.064953	0.035456	-0.05899
O19	-0.30951	-0.267920	-0.424950	0.041589	0.115438	0.078514	-0.07385
O20	-0.36853	-0.376070	-0.536300	-0.007540	0.167766	0.080114	-0.17531

philic attack. The nucleophilic sites in the 5FUTU cocrystal are arranged in the following sequence, with a positive value ($\Delta f(r) > 0$): S8 > C1 > H3 > N15 > H4 > N5 > H7. These values are shown in Table-8. Likewise, O20 > C10 > C13 > H6 > F14 > O19 > H11 > N17 > H18 > H16 > C12 > C9 > N2 (*i.e.*, $\Delta f(r) < 0$) is the negative value of the electrophilic attack site. The local behaviour of molecules controls their behaviour as electrophiles or nucleophiles during a process.

NMR studies: The experimental and DFT-calculated ^{13}C and ^{1}H NMR chemical shifts of the 5FUTU cocrystal are compared in Fig. 15, with the corresponding values shown in Table-9. The ^{13}C NMR spectrum shows the highest experimental shift at C1 (181.93 ppm), when compared with the calculated value of 191.89 ppm. The experimental shifts for C13, C9, C12 and C10 are 160.42, 151.51, 141.78 and 139.50 ppm, respectively, while the corresponding calculated values are 162.09, 151.09, 147.34 and 133.24 ppm. The high chemical shift at C1 is consistent with its bonding environment involving S8, O2 and O5. In the ^{1}H NMR spectrum, H11 and H18 exhibit the highest experimental shifts, at 7.59 and 7.58 ppm, respectively, compared with calculated values of 7.34 and 7.29 ppm. The agreement between experimental and GIAO-calculated chemical shifts supports the proposed molecular structure of the 5FUTU cocrystal [57].

Energy framework calculation: The energy framework was used to examine the intermolecular interactions governing crystal packing in 5FUTU with electrostatic, polarization, dispersion, repulsion and total interaction energies evaluated using CrystalExplorer. Pairwise interaction energies were calculated for molecules within a 3.8 Å radius of the reference molecule. Fig. 16 displays the Coulomb (red), dispersion (green) and total interaction energies (blue) along the crystallographic a, b and c axes. The reported energy components are -323.8 kJ mol^{-1} for electrostatic interactions, -81.8 kJ mol^{-1} for polarization, -145.5 kJ mol^{-1} for dispersion and +358.0 kJ mol^{-1} for repulsion. Electrostatic interactions make the largest attractive

TABLE 9
CALCULATED AND EXPERIMENTAL ppm RANGE OF 5FUTU OBSERVED *via* NMR ANALYSIS

Atoms	Calculated (shielding, ppm)	Experimental (ppm)
C1	191.89	181.93
C13	162.09	160.42
C9	151.09	151.51
C12	147.34	141.78
C10	133.24	139.5
H11	7.34	7.59
H18	7.29	7.58
H3	7.04	–
H6	6.62	–
H16	6.47	–
H4	5.3	–
H7	5.27	–

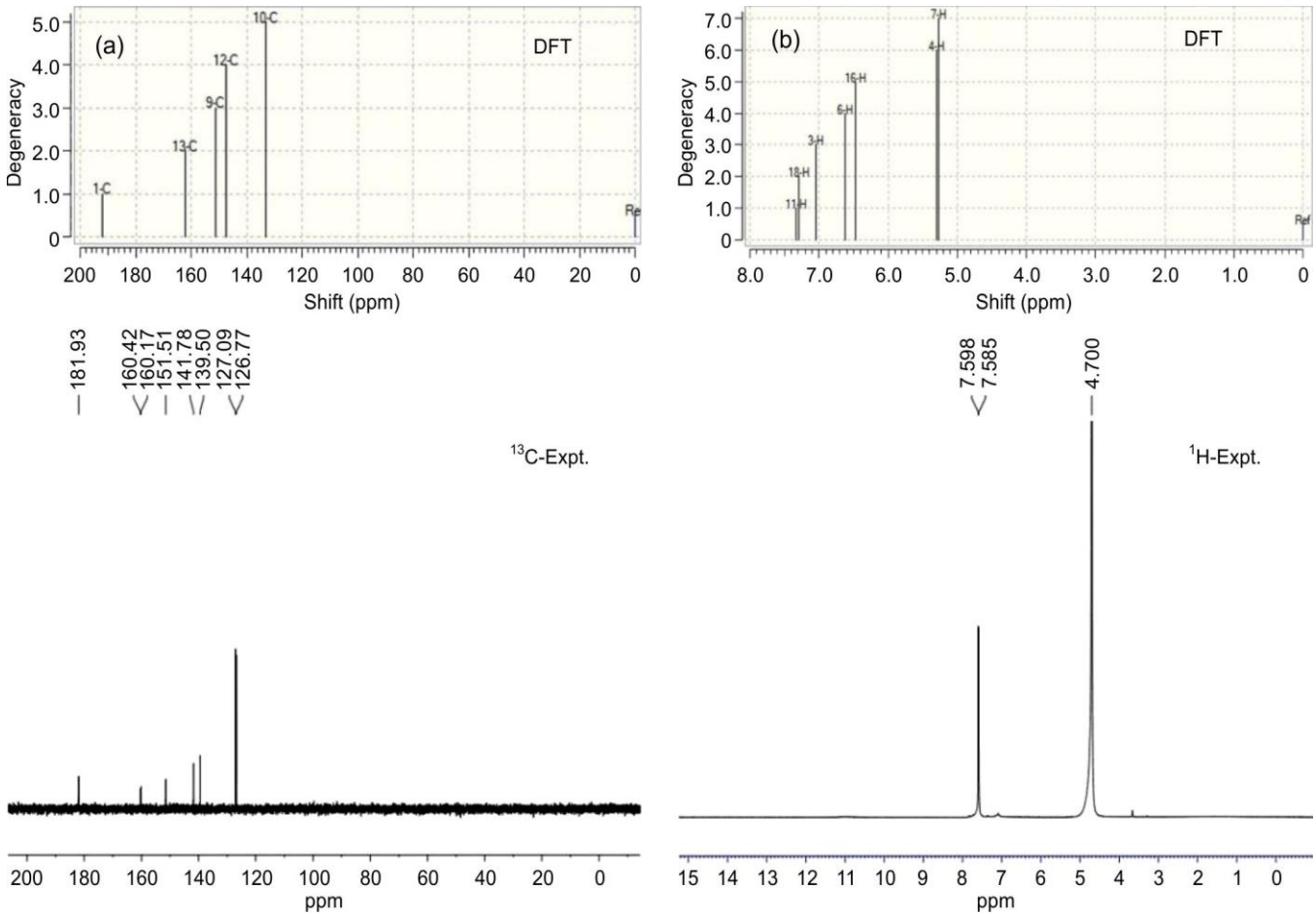


Fig. 15. NMR spectra analysis of 5FUTU cocrystal with (a) ^{13}C and (b) ^{1}H

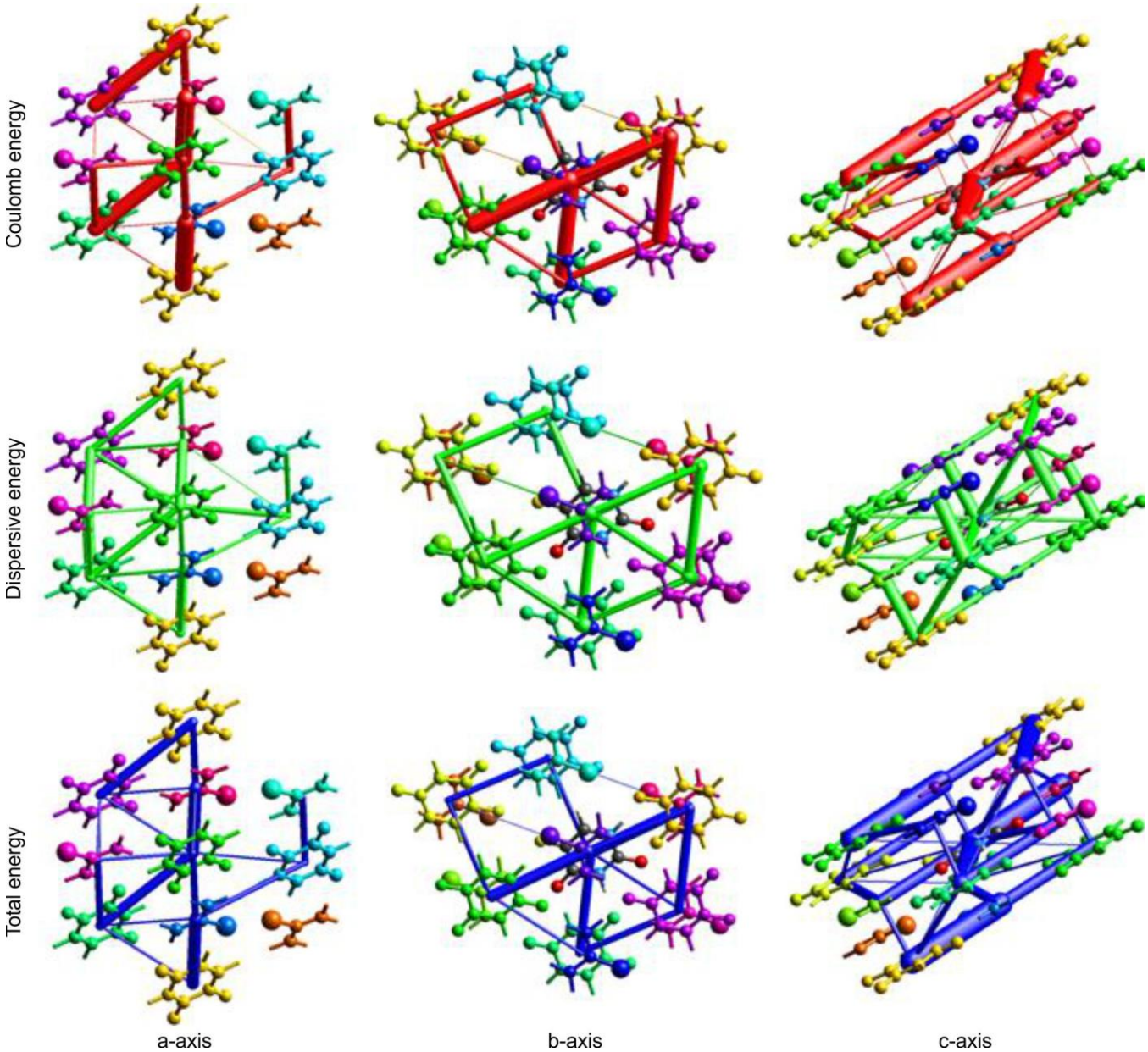


Fig. 16. Pictorial representation of Coulomb, dispersion and total interaction energies along the *a*-, *b*- and *c*-axes of the 5FUTU crystal structure

contribution, followed by dispersion and polarization. The corresponding scale factors are 1.057, 0.740, 0.871 and 0.618 for electrostatic, polarization, dispersion and repulsion terms, respectively. Pairwise interaction energies are listed in Table-10. The orange-highlighted molecular pair has a slightly positive total interaction energy of +2.4 kJ mol^{-1} at a centroid separation of 6.93 Å, which is consistent with a weakly repulsive interaction. The magenta-highlighted pair has the most negative total interaction energy, -63.1 kJ mol^{-1}, at a centroid separation of 5.43 Å, which makes it the strongest stabilizing contact among the pairs analyzed.

Molecular docking studies: Molecular docking was performed to examine the binding of the 5FUTU cocrystal to five cancer-related protein targets associated with breast cancer *viz*. EGFR, PARP, GSK-3β, AKT and BCL2. GSK-3β exhibited the most favourable docking score (-6.6 kcal mol^{-1}) followed by AKT and PARP (-6.3 kcal mol^{-1}), EGFR (-5.9 kcal mol^{-1}) and BCL2 (-5.7 kcal mol^{-1}). The predicted binding poses and intermolecular contacts were examined using BIOVIA Discovery Studio and are shown in Fig. 17.

The 5FUTU–GSK-3β complex contained nine reported hydrogen-bond contacts, comprising seven conventional and two carbon-type hydrogen bonds, along with one halogen interaction and one hydrophobic contact. The hydrogen-bond contacts involved SER338, ALA336, GLU333 and ASP341, with reported distances ranging from 2.5754 to 3.0428 Å. The halogen and hydrophobic contacts involved ALA336, at 3.0805 and 5.125 Å, respectively. The 5FUTU–AKT complex exhibited six conventional hydrogen bonds involving ARG-273, THR82, ASP292, TYR272, CYS296 and ASP274, together with one π-anion interaction. The reported contact distances ranged from 2.0537 to 3.6563 Å.

TABLE-10
INTERMOLECULAR INTERACTION ENERGIES (kJ mol^{-1}) OF SELECTED MOLECULAR PAIRS WITHIN THE 5FUTU CRYSTAL PACKING, CALCULATED AT THE B3LYP/6-311++G(d,p) LEVEL USING CRYSTALEXPLORER

	N	Symop	R	Electron density	E_ele	E_pol	E_dis	E_rep	E_tot
	0	–	6.13	B3LYP/6-31G(d,p)	-40.1	-7.8	-10.2	35.9	-34.9
	1	–	6.93	B3LYP/6-31G(d,p)	3.9	-0.8	-2.0	1.0	2.4
	2	x, y, z	7.25	B3LYP/6-31G(d,p)	-3.1	-0.8	-2.1	0.0	-5.7
	1	-x, -y, -z	7.91	B3LYP/6-31G(d,p)	-4.4	-0.3	-2.5	0.3	-6.8
	1	–	6.13	B3LYP/6-31G(d,p)	-40.1	-7.8	-10.2	35.9	-34.9
	2	x, y z	6.16	B3LYP/6-31G(d,p)	1.0	-1.4	-6.4	1.3	-4.7
	1	-x, -y, -z	5.52	B3LYP/6-31G(d,p)	-78.6	-18.5	-14.3	95.5	-50.2
	1	–	5.79	B3LYP/6-31G(d,p)	-25.7	-5.2	-7.2	17.4	-26.5
	1	-x, -y, -z	5.71	B3LYP/6-31G(d,p)	-3.6	-2.5	-11.8	7.2	-11.4
	1	–	3.46	B3LYP/6-31G(d,p)	-3.6	-4.9	-23.2	22.4	-13.9
	1	–	5.55	B3LYP/6-31G(d,p)	-5.3	-1.7	-7.4	2.9	-11.5
	1	–	3.88	B3LYP/6-31G(d,p)	-4.0	-4.3	-20.6	18.3	-14.1
	1	-x, -y, -z	5.99	B3LYP/6-31G(d,p)	-8.1	-1.8	-10.3	6.1	-15.1
	1	–	6.75	B3LYP/6-31G(d,p)	-22.7	-6.0	-5.6	24.8	-18.1
	1	–	5.43	B3LYP/6-31G(d,p)	-89.4	-18.0	-11.7	89.0	-63.1

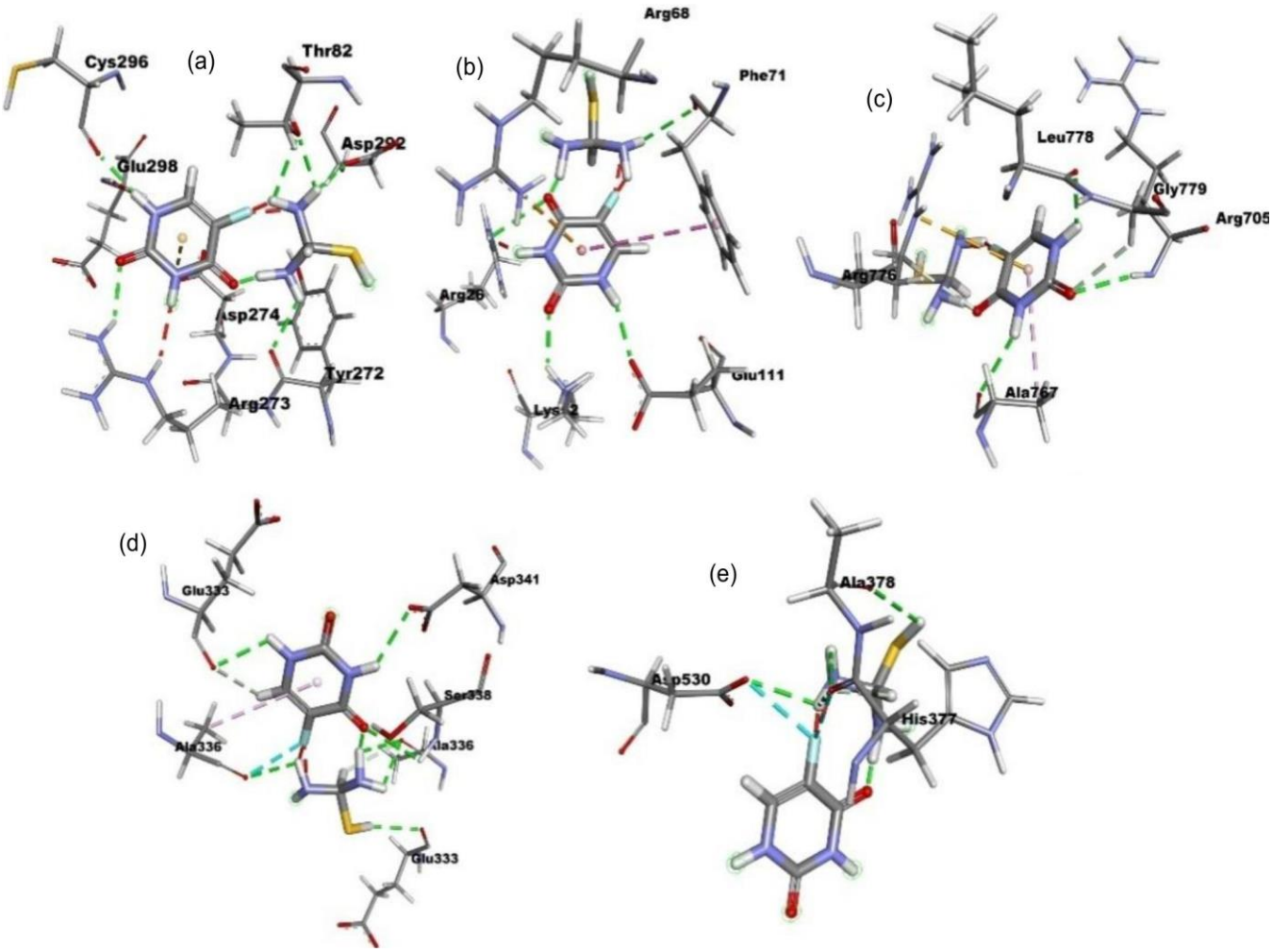


Fig. 17. Two-dimensional images of molecular docking interactions between 5FUTU and the target proteins

The 5FUTU–PARP complex showed five hydrogen-bond contacts, which comprise four conventional and one carbon-type hydrogen bond, along with two halogen interactions. The reported interacting residues were ASP530, HIS377, and ALA378 with contact distances ranging from 2.4445 to 2.9389 Å. In the 5FUTU–EGFR complex, five hydrogen-bond contacts were reported alongside one π-cation interaction and one π-alkyl contact. These interactions involved ARG705, LEU778, ALA767, ARG776 and GLY779, with hydrogen-bond distances between 2.2298 and 2.8305 Å. The 5FUTU–BCL2 complex exhibited four hydrogen bonds involving LYS22, ARG26, PHE71 and GLU111, together with a π-cation interaction involving ARG68 and a π–π T-shaped interaction involving PHE71. The reported contact distances ranged from 2.1303 to 5.3420 Å. These docking results describe the predicted binding poses and contacts of 5FUTU within the selected protein binding sites.

MTT assay: The cytotoxic effects of the 5FUTU co-crystal were evaluated in MDA-MB-231 triple-negative breast cancer cells using the MTT assay [58]. The cells were treated with 5FUTU or free 5FU at concentrations ranging from 10 to 80 μM for 24 h. Fig. 18a presents the cell viability results for 5FUTU, while Fig. 18c shows the corresponding morphological changes in treated cells. The cell viability following 5FUTU treatment decreased from 82.49% at 10 μM to 25.64% at 80 μM. The intermediate concentrations of 20, 30, 40, 50, 60, and 70 μM resulted in cell viabilities of 75.17%, 61.86%, 52.35%, 45.91%, 37.55% and 30.68%, respectively. The calculated IC_{50} of 5FUTU was 46.7 μM. Free 5FU was tested under the same conditions for comparison (Fig. 18b), yielding an IC_{50} of 62.1 μM. The lower IC_{50} of 5FUTU indicates greater *in vitro* cytotoxic potency than free 5FU under the tested conditions.

Pharmacokinetic analysis: The physico-chemical properties, pharmacokinetic predictions and drug-likeness descriptors of 5FU and the 5FUTU system were evaluated using SwissADME, with the results shown in Table-11. The molecular weight increased from 130.08 g mol^{-1} for 5FU to 210.23 g mol^{-1} for 5FUTU, accompanied by an increase in heavy atoms from 9 to 13. The fraction of Csp^3-hybridized carbon atoms increased from 0.0 to 0.6. The numbers of hydrogen-bond donors and acceptors increased from 2 to 4 and from 3 to 5, respectively. The topological polar surface area (TPSA) increase from 65.72 to 149.04 $Å^2$, while molar refractivity increased from 27.64 to 53.77. The consensus LogP decreased from 0.13 for 5FU to -0.96 for 5FUTU, which is consistent with lower predicted lipophilicity. The ESOL model estimated aqueous solubilities of 34.3 mg mL^{-1} for 5FU and 197 mg mL^{-1} for 5FUTU; the Ali and SILICOS-IT models were also used to assess solubility. Both compounds were predicted to have no blood-brain barrier permeability and were not classified as P-glycoprotein substrates. The SwissADME predictions further classified both compounds as non-inhibitors of the major cytochrome P450 enzymes. The predicted skin permeability coefficient (log Kp) decreased from -7.73 for 5FU to -8.84 for 5FUTU, consistent with lower predicted skin permeability. The drug-likeness screening showed no PAINS alerts for either structure and both met Lipinski's rule

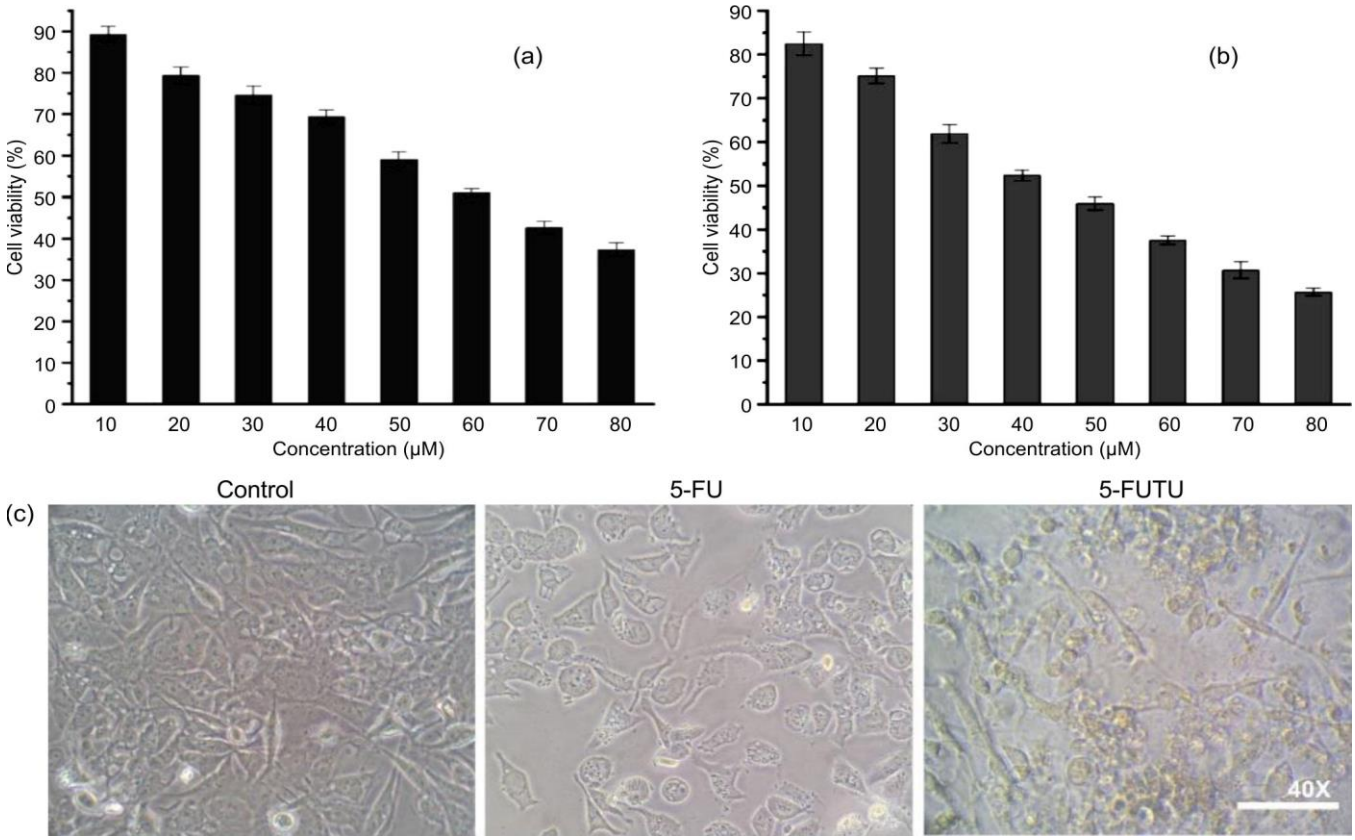


Fig. 18. Cell viability of MDA-MB-231 cells treated with (a) 5FU, (b) 5FUTU cocrystal and (c) morphological changes in cells

TABLE-11
ANALYZED PHARMACOKINETICS
PARAMETERS OF 5FU AND 5FUTU COCRYSTAL

Parameters	5FU	5FUTU
Canonical SMILES	FC1C[nH]C(=O)[nH]C1=O	FC1CNC(=O)NC1=O.NC(S)N
Formula	$C_4H_3FN_2O_2$	$C_5H_{11}FN_4O_2S$
MW	130.08	210.23
#Heavy atoms	9	13
#Aromatic heavy atoms	6	0
Fraction Csp^3	0	0.6
#Rotatable bonds	0	0
#H-bond acceptors	3	5
#H-bond donors	2	4
MR	27.64	53.77
TPSA	65.72	149.04
iLOGP	0.44	0.41
XLOGP3	-0.89	-1.77
WLOGP	-0.38	-2.06
MLOGP	-0.32	-1.57
Silicos-IT Log P	1.78	0.2
Consensus Log P	0.13	-0.96
ESOL Log S	-0.58	-0.03
ESOL solubility (mg/mL)	3.43E+01	1.97E+02
ESOL solubility (mol/L)	2.64E-01	9.37E-01
ESOL class	Very soluble	Very soluble
Ali Log S	-0.01	-0.84
Ali solubility (mg/mL)	1.28E+02	3.01E+01
Ali solubility (mol/L)	9.82E-01	1.43E-01
Ali class	Very soluble	Very soluble
Silicos-IT LogSw	-1.71	-0.88
Silicos-IT solubility (mg/mL)	2.54E+00	2.75E+01
Silicos-IT solubility (mol/L)	1.95E-02	1.31E-01
Silicos-IT class	Soluble	Soluble
GI absorption	High	Low
BBB permeant	No	No
Pgp substrate	No	No
CYP1A2 inhibitor	No	No
CYP2C19 inhibitor	No	No
CYP2C9 inhibitor	No	No
CYP2D6 inhibitor	No	No
CYP3A4 inhibitor	No	No
log Kp (cm/s)	-7.73	-8.84
Lipinski #violations	0	0
Ghose #violations	3	1
Veber #violations	0	1
Egan #violations	0	1
Muegge #violations	2	0
Bioavailability Score	0.55	0.55
PAINS #alerts	0	0
Brenk #alerts	0	2
Leadlikeness #violations	1	1
Synthetic accessibility	1.52	2.42

of five. The 5FUTU structure had fewer Ghose and Muegge filter violations than 5FU. Its synthetic accessibility score was 2.42, while both compounds had a bioavailability score of 0.55. The radar plot (Fig. 19) shows the comparative physicochemical profiles. These computational results identify differences in the predicted properties of the structures submitted to SwissADME and support further investigation of solubility and formulation behaviour.

Conclusion

The 5-fluorouracil–thiourea (5FUTU) cocrystal was synthesized and its crystal structure was confirmed by X-ray diffraction. Experimental FTIR, UV-Vis and NMR data were compared with theoretical results, with good agreement between the measured and calculated values. DFT calculations were used to examine the molecular geometry, vibrational modes, and electronic properties. The experimental UV-Vis absorption maximum at 270 nm differed from the TD-DFT-predicted transition at 303 nm, assigned to a $\pi \rightarrow \pi^*$ transition.

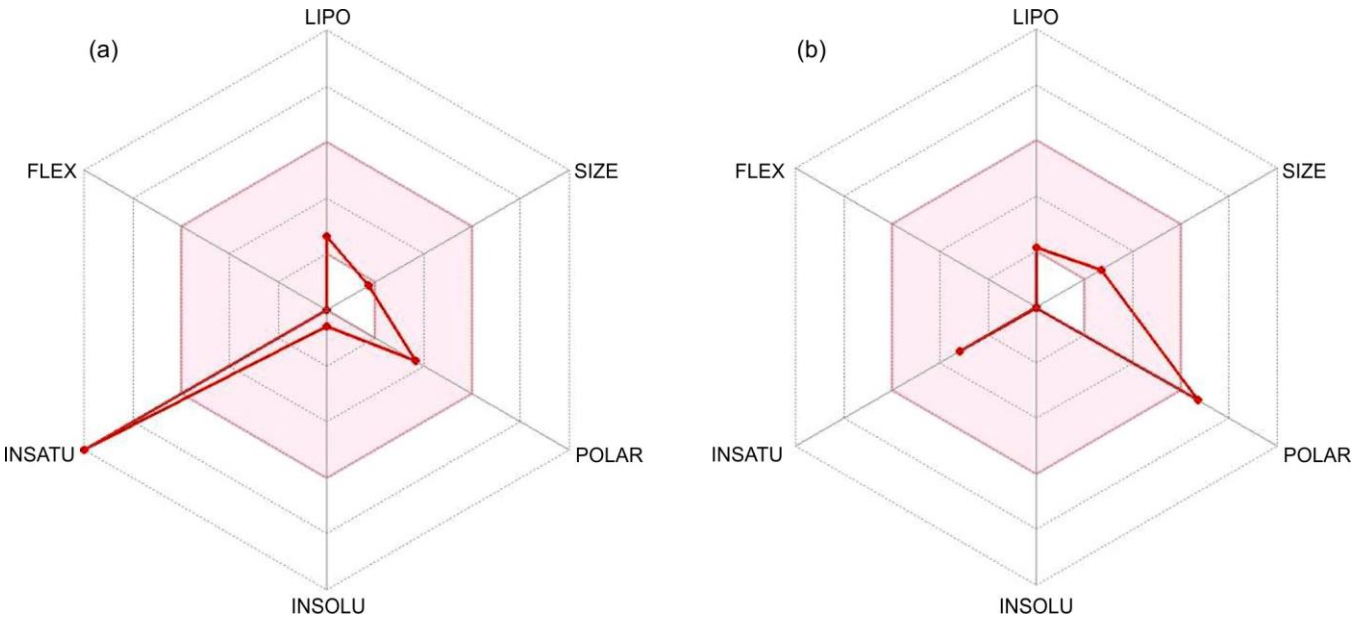


Fig. 19. SwissADME bioavailability radar plots of (a) 5FU and (b) 5FUTU cocrystal

Hirshfeld surface analysis and two-dimensional fingerprint plots characterized the intermolecular contacts within the crystal packing. The calculated HOMO–LUMO gap was 2.5249 eV, while Mulliken charge analysis, natural population analysis, NBO analysis, ELF, LOL and RDG calculations provided further insight into the charge distribution, bonding, electron localization and non-covalent interactions. Molecular docking against five breast cancer-related protein targets yielded scores ranging from -5.7 to -6.6 kcal mol^{-1}. In the MTT assay, 5FUTU exhibited an IC_{50} of 46.7 µM against MDA-MB-231 cells after 24 h, compared with 62.1 µM for free 5FU, which indicae higher cytotoxic potency under the tested conditions. SwissADME predictions identified differences in the physico-chemical and drug-likeness descriptors of the submitted 5FUTU representation relative to 5FU, although these predictions require experimental validation. The findings provide a basis for further investigation of 5FUTU as a potential anticancer formulation.

ACKNOWLEDGEMENTS

The authors thank Biomaz Infosearch, Madurai for their technical support in this study. The authors also thank Kalasalingam Academy of Research and Education for providing the University Research Fellowship to one of the authors, J.K.

CONFLICT OF INTEREST

The authors declare that there is no conflicts of interest regarding the publication of this article.

DECLARATION OF AI-ASSISTED TECHNOLOGIES

During the preparation of this manuscript, the authors used an AI-assisted tool(s) to improve the language and no data, results or scientific conclusions were generated by AI. All analyses, interpretations and conclusions are the authors' own. The authors reviewed and edited the content and take full responsibility for the published work.

REFERENCES

1. A. Kumar, A.K. Singh, H. Singh, V. Vijayan, D. Kumar, J. Naik, S. Thareja, J.P. Yadav, P. Pathak, M. Grishina, A. Verma, H. Khalilullah, M. Jaremko, A.-H.M. Emwas and P. Kumar, *Pharmaceuticals*, **16**, 299 (2023); https://doi.org/10.3390/ph16020299
2. D.K. Lang, R. Kaur, R. Arora, B. Saini and S. Arora, *Anti-Cancer Agents Med. Chem.*, **20**, 2150 (2020); https://doi.org/10.2174/1871520620666200705214917
3. J. Akhtar, A.A. Khan, Z. Ali, R. Haider and Y.S. Yar, *Eur. J. Med. Chem.*, **125**, 143 (2017); https://doi.org/10.1016/j.ejmech.2016.09.023
4. F. Jubeen, A. Liaqat, M. Sultan, S. Zafar Iqbal, I. Sajid and F. Sher, *Saudi Pharm. J.*, **27**, 1164 (2019); https://doi.org/10.1016/j.jsps.2019.09.013
5. S. Hong, W. Cai, Z. Huang, Y. Wang, X. Mi, Y. Huang, Z. Lin and X. Chen, *Oncol. Rep.*, **44**, 1333 (2020); https://doi.org/10.3892/or.2020.7728
6. B. Ewert de Oliveira, O.H. Junqueira Amorim, L.L. Lima, R.A. Rezende, N.C. Mestnik, E. Bagatin and G.R. Leonardi, *J. Drug Deliv. Sci. Technol.*, **61**, 102155 (2022); https://doi.org/10.1016/j.jddst.2020.102155
7. C. Sethy and C.N. Kundu, *Biomed. Pharmacother.*, **137**, 111285 (2021); https://doi.org/10.1016/j.biopha.2021.111285
8. J. Gu, Z. Li, J. Zhou, Z. Sun and C. Bai, *Oncol. Lett.*, **18**, 2091 (2019); https://doi.org/10.3892/ol.2019.10474
9. E. Stoler and J.C. Warner, *Molecules*, **20**, 14833 (2015); https://doi.org/10.3390/molecules200814833
10. X.L. Dai, S. Li, J.M. Chen and L.B. Lu, *Cryst. Growth Des.*, **16**, 4430 (2016); https://doi.org/10.1021/acs.cgd.6b00552
11. A. Delori, M.D. Eddleston and W. Jones, *CrystEngComm*, **15**, 73 (2013); https://doi.org/10.1039/C2CE26147B
12. M.K. Gautam, M. Besan, D. Pandit, S. Mandal and R. Chadha, *AAPS PharmSciTech*, **20**, 149 (2019); https://doi.org/10.1208/s12249-019-1360-9
13. F. Jubeen, A. Liaqat, F. Amjad, M. Sultan, S.Z. Iqbal, I. Sajid, M.B. Khan Niazi and F. Sher, *Cryst. Growth Des.*, **20**, 2406 (2020); https://doi.org/10.1021/acs.cgd.9b01570
14. N.I. Nadzri, N.H. Sabri, V.S. Lee and S.N. Abdul Halim, *J. Chem. Crystallogr.*, **46**, 144 (2016); https://doi.org/10.1007/s10870-016-0638-y
15. M.J. Frisch, G.W. Trucks, H.B. Schlegel, G.E. Scuseria, M.A. Robb, J.R. Cheeseman and D.J. Fox, Gaussian 09, Revision D.01, Gaussian, Inc., Wallingford CT (2009).
16. R. Dennington, T. Keith and J. Millam, GaussView, Version 5, Semichem Inc., Shawnee Mission, KS (2009).
17. A.D. Becke, *J. Chem. Phys.*, **98**, 5648 (1993); https://doi.org/10.1063/1.464913
18. C. Lee, W. Yang and R.G. Parr, *Phys. Rev. B Condens. Matter*, **37**, 785 (1988); https://doi.org/10.1103/PhysRevB.37.785
19. M.H. Jamroz, Vibrational Energy Distribution Analysis VEDA 4.0 Program, Warsaw (2004).
20. S.P. Vijaya Chamundeeswari, E.R.J. Jebaseelan Samuel and N. Sundaraganesan, *Eur. J. Chem.*, **2**, 136 (2011); https://doi.org/10.5155/eurjchem.2.2.136-145.169
21. E.D. Glendening, A.E. Reed, J.E. Carpenter and F. Weinhold, NBO, Version 3.1, Gaussian Inc., Pittsburgh, PA (2003).
22. T. Koopmans, *Physica*, **1**, 104 (1934); https://doi.org/10.1016/S0031-8914(34)90011-2
23. L. Pauling, The Nature of the Chemical Bond, Cornell University Press, Ithaca, New York, (1965).
24. F.M. Anjalin, N. Kanagathara, M.K. Marchewka and V. Mohankumar, *J. Mol. Struct.*, **1183**, 78 (2019); https://doi.org/10.1016/j.molstruc.2019.01.051
25. A. Zochedh, M. Priya, A. Shunmuganarayanan, A.B. Sultan and T. Kathiresan, *J. Mol. Struct.*, **1282**, 135113 (2023); https://doi.org/10.1016/j.molstruc.2023.135113
26. G. Varsanyi, Assignments for Vibrational Spectra of Seven Hundred Benzene Derivatives, Academic Kiado (1973).
27. G. Thilagavathi and M. Arivazhagan, *Spectrochim. Acta A Mol. Biomol. Spectrosc.*, **79**, 389 (2011); https://doi.org/10.1016/j.saa.2011.01.052
28. R. Gayathri and M. Arivazhagan, *Spectrochim. Acta A Mol. Biomol. Spectrosc.*, **81**, 242 (2011); https://doi.org/10.1016/j.saa.2011.06.005
29. M. Karabacak, E. Postalcilar and M. Cinar, *Spectrochim. Acta A Mol. Biomol. Spectrosc.*, **85**, 261 (2012); https://doi.org/10.1016/j.saa.2011.10.003
30. B.C. Smith, Infrared Spectral Interpretation: A Systematic Approach, CRC Press (2018).
31. M. Khalid, A. Ali, J. Tariq, M.N. Tahir, H.A.R. Aliabad, I. Hussain, M. Ashfaq and M.U. Khan, *ChemistrySelect*, **5**, 10618 (2020); https://doi.org/10.1002/slct.202002653
32. M. Arivazhagan, S. Prabhakaran and R. Gayathri, *Spectrochim. Acta A Mol. Biomol. Spectrosc.*, **82**, 332 (2011); https://doi.org/10.1016/j.saa.2011.07.057
33. V. Vimalraj, S. Vijayalakshmi, S. Umayaparvathi and A.R. Krishnan, *Spectrochim. Acta A Mol. Biomol. Spectrosc.*, **78**, 670 (2011); https://doi.org/10.1016/j.saa.2010.11.045
34. B. Revathi, V. Balachandran, B. Raja, K. Anitha and M. Kavimani, *J. Mol. Struct.*, **1141**, 81 (2017); https://doi.org/10.1016/j.molstruc.2017.03.078
35. B.C. Smith, Infrared Spectral Interpretation: A Systematic Approach, CRC Press, Washington, DC (1998).

36. J.C. Dobrowolski, J.E. Rode, R. Kołos, M.H. Jamróz, K. Bajdor and A.P. Mazurek, *J. Phys. Chem. A*, **109**, 2167 (2005); https://doi.org/10.1021/jp045213f
37. E. Bednarek, J.C. Dobrowolski, K. Dobrosz-Teperek, L. Kozerski, W. Lewandowski and A.P. Mazurek, *J. Mol. Struct.*, **554**, 233 (2000); https://doi.org/10.1016/S0022-2860(00)00670-0
38. V.K. Rastogi, M.A. Palafox, R.P. Tanwar and L. Mittal, *Spectrochim. Acta A Mol. Biomol. Spectrosc.*, **58**, 1987 (2002); https://doi.org/10.1016/S1386-1425(01)00650-3
39. R.K. Srivastava, V. Narayan, O. Prasad and L. Sinha, *J. Chem. Pharm. Res.*, **4**, 3287 (2012).
40. T.K. Kuruvilla, J.C. Prasana, S. Muthu, J. George and S.A. Mathew, *Spectrochim. Acta A Mol. Biomol. Spectrosc.*, **188**, 382 (2018); https://doi.org/10.1016/j.saa.2017.07.029
41. F. Weinhold and J.E. Carpenter, In eds.: R. Ruoff, The Structure of Small Molecules and Ions, Springer, Boston, pp. 227-236 (1988).
42. M. Snehalatha, C. Ravikumar, I. Hubert Joe, N. Sekar and V.S. Jayakumar, *Spectrochim. Acta A Mol. Biomol. Spectrosc.*, **72**, 654 (2009); https://doi.org/10.1016/j.saa.2008.11.017
43. C. James, A.A. Raj, R. Reghunathan, V.S. Jayakumar and I.H. Joe, *J. Raman Spectrosc.*, **37**, 1381 (2006); https://doi.org/10.1002/jrs.1554
44. J.N. Liu, Z.R. Chen and S.F. Yuan, *J. Zhejiang Univ. Sci. B*, **6**, 584 (2005); https://doi.org/10.1631/jzus.2005.B0584
45. E.I. Paulraj and S. Muthu, *Spectrochim. Acta A Mol. Biomol. Spectrosc.*, **108**, 38 (2013); https://doi.org/10.1016/j.saa.2013.01.061
46. B. Silvi and A. Savin, *Nature*, **371**, 683 (1994); https://doi.org/10.1038/371683a0
47. T. Lu and F. Chen, *J. Comput. Chem.*, **33**, 580 (2012); https://doi.org/10.1002/jcc.22885
48. H. Jacobsen, *Can. J. Chem.*, **86**, 695 (2008); https://doi.org/10.1139/v08-052
49. J.S. Murray and K. Sen, Molecular Electrostatic Potentials: Concepts and Applications (1996).
50. J.M. Seminario, Recent Developments and Applications of Modern Density Functional Theory, Elsevier Science (1996).
51. A. Zochedh, M. Priya, C. Chakaravarthy, A.B. Sultan and T. Kathiresan, *Polycycl. Aromat. Compd.*, **43**, 6516 (2023); https://doi.org/10.1080/10406638.2022.2118332
52. E.R. Johnson, S. Keinan, P. Mori-Sánchez, J. Contreras-García, A.J. Cohen and W. Yang, *J. Am. Chem. Soc.*, **132**, 6498 (2010); https://doi.org/10.1021/ja100936w
53. R.A. Boto, J.P. Piquemal and J. Contreras-García, *Theor. Chem. Acc.*, **136**, 139 (2017); https://doi.org/10.1007/s00214-017-2169-9
54. J.R. Lane, J. Contreras-García, J.P. Piquemal, B.J. Miller and H.G. Kjaergaard, *J. Chem. Theory Comput.*, **9**, 3263 (2013); https://doi.org/10.1021/ct400420r
55. A.A. Khan, R. Ahmad and I. Ahmad, *J. Mol. Liq.*, **309**, 113008 (2020); https://doi.org/10.1016/j.molliq.2020.113008
56. W. Yang and W.J. Mortier, *J. Am. Chem. Soc.*, **108**, 5708 (1986); https://doi.org/10.1021/ja00279a008
57. C. Morell, A. Grand and A. Toro-Labbé, *J. Phys. Chem. A*, **109**, 205 (2005); https://doi.org/10.1021/jp046577a
58. A. Zochedh, K. Chandran, K. Arumugam, B.A. Al-Asbahi, A.B. Sultan, Y.A. Kumar, M. Priya and T. Kathiresan, *Chem. Afr.*, **7**, 5367 (2024); https://doi.org/10.1007/s42250-024-01133-8